Research Paper

Proprioceptive swarms for celestial body exploration

Simone Cottiga, Matteo Caruso, Paolo Gallina, Stefano Seriani *

Department of Engineering and Architecture, University of Trieste, via A. Valerio 6/1, Trieste, 34127, Italy

ARTICLE INFO

ABSTRACT

The exploration of small celestial bodies has been a very active field ever since the dawn of space exploration. However, traditional approaches based on monolithic landers allow only the area in the immediate vicinity to the landing spot to be examined. Using mobile systems like rovers allow for better coverage, but at considerable cost and complexity. In this work, we propose an approach based on swarms of small nonmaneuverable agents, equipped with a sensor package, that are launched from a base station and made to land across the entire surface of the asteroid or comet. The methodology is based on multilateration using small range-finding radio frequency sensors aboard the agents; this enables position determination relative to the base station. Through dynamics simulation, we show that this approach is feasible even in highly irregular gravity fields where closed-form solutions for orbital mechanics are not available, such as the case of comet 67P/Churyumov–Gerasimenko. We show a sensitivity analysis of the absolute position error of the agents which originated from range-measurement error. The surface coverage is evaluated against the numerosity of the swarm. Finally, we show that allowing for a subset of agents to follow a long-period orbit around the object enables better localization of the landed agents, thus increasing the overall performance.

1. Introduction

Exploring the surface of *Small Celestial Bodies* (SCB), such as asteroids and comets, has recently become the subject of widespread attention, following a series of very successful missions from the major space agencies [1,2]. However, even since the Galileo mission, launched in 1989, which visited the asteroids Ida and Gaspra, and the even earlier Pioneer 10 mission with its incidental Flyby of two small asteroids (the latter is 307 Nike, while the former remains unknown), it became apparent that SCBs promised to be a potential target for exploration. It is agreed that understanding the physical and dynamical characteristics, distribution, development, and evolution of tiny bodies is essential to understanding how planets were formed [3–5]. It is also crucial to determine whether and how these objects may have contributed to the emergence of life on Earth [6].

The ICE mission, launched in 1978 to comet 21P/Giacobini–Zinner and – most notably – 1P/Halley, marked the start of early small-body exploration. It is the NEAR Shoemaker mission (launch 1996) the turning point, where exploration became truly *in-situ*. For the first time, an orbiter and lander were deployed on a small body, the minor planet 433 Eros. In 1999 NASA's Stardust mission was launched; in 2004, it captured a small quantity of cometary particles from the tail of 81P/Wild, which, in 2006, were delivered to Earth via capsule. In 2003 JAXA's Hayabusa mission [6] was the first instance where

a probe was able to land, grab a sample of soil, and fly back to Earth — the first arguably proper sample-return mission. Several other missions followed and presented a wide range of mission architectures, scope, and capabilities. For example, the Deep Impact mission launched by NASA to comet 9P/Tempel, was equipped with an impactor that was sent to the surface with a velocity of $10.2\,\mathrm{km\,s^{-1}}$. The Rosetta mission was sent to comet Churyumov–Gerasimenko in 2004 by ESA, and was equipped with the Philae lander. This was supposed to land and anchor to the surface, objectives which it only partially fulfilled. The DAWN probe [7], launched in 2007, was the first to orbit two extraterrestrial bodies: Vesta and Ceres; it provided insight into two of the largest asteroid belt objects. In 2014, JAXA sent the Hayabusa 2 mission [8] to near-Earth asteroid 162173 Ryugu; the spacecraft hosted four small rovers: HIBOU, OWL, MASCOT and MINERVA-II-2. Only the first three were fully successful, the fourth having failed its deployment. Similarly to the Hayabusa mission, in 2016 NASA launched the OSIRIS-REx mission [9] to near-Earth asteroid 101955 Bennu, which successfully collected a sample from the superficial soil of the object and returned it to Earth. DART, launched in 2021 and operated by NASA, was the first mission to investigate orbit modification via kinetic impactor [10], which it successfully did in 2022 on the binary asteroid 65803 Didymos. The year 2021 brought us the launch of NASA's Lucy
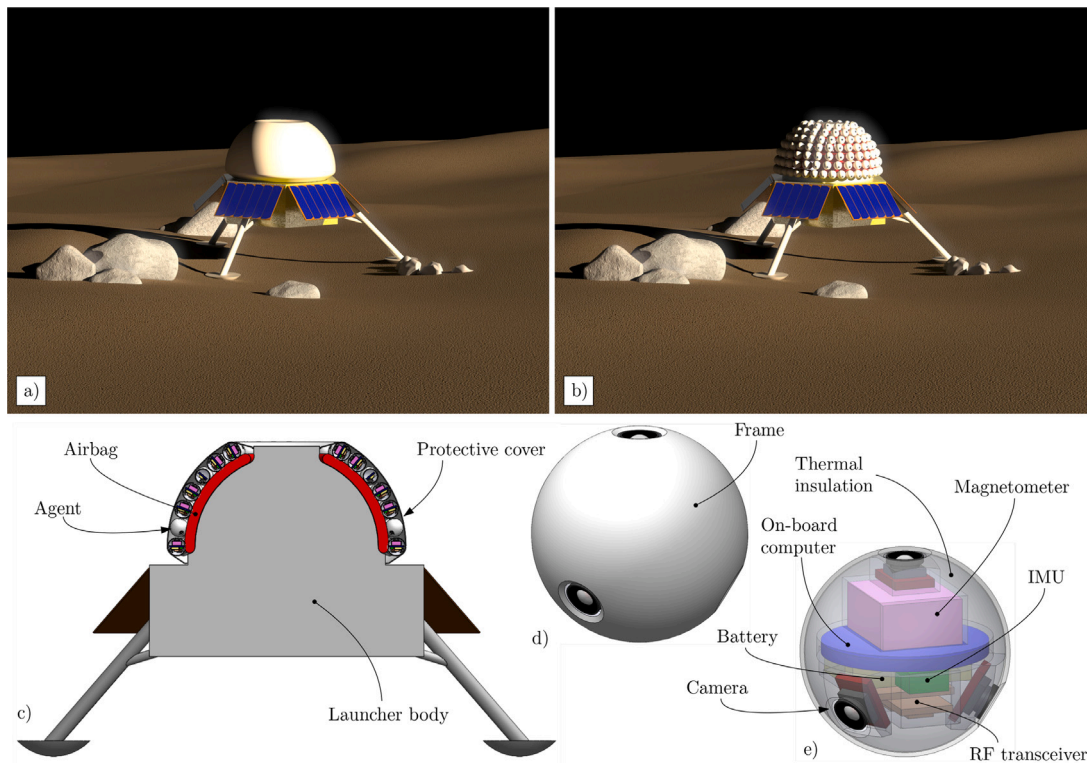
Fig. 1. Conceptual view of the system. (a) Impression of the full system in context. (b) Impression of the system without the cover, showing the arrangement of the sensors. (c) Section of the lander, showing the main components related to this work. (d) External view of a single agent. (e) Internal view of an agent, highlighting the main components.

mission [11], expected to visit no less than seven different asteroids in twelve years; two targets belong to the main belt and six are Jupiter Trojans. In 2023, the Psyche orbiter [12] will be sent to 16 Psyche, while in 2024 the Hera spacecraft [13] will start its travel towards 65803, to further propel the investigation that was started with DART. The China National Space Administration (CNSA) is developing the Tianwen-2 sample-return mission [14] for near-Earth asteroid 469219 Kamo'oalewa and comet 311P/PANSTARRS. Following in the footsteps of the DART mission, the CNSA is working on an unnamed asteroid deflection test to be launched in 2026 and to target asteroid 2020 PN1. ESA and JAXA are currently working on the "Comet interceptor" [15], which is scheduled for 2029.

While our primary focus is on proposing a methodology for the exploration of a SCB based on a swarm of small satellites, in this paper we provide a brief overview of past missions to celestial bodies, in chronological order, in Table 1, to provide readers with a contextual understanding of the historical progression of SCB exploration. Moreover, by highlighting the absence of similar work in the existing literature, this table highlights the contribution of our work in filling this gap.

As introduced above, our work is focused on proposing a methodology for the exploration of an SCB based on a swarm of small agents that is launched by a lander (Fig. 1). The lander, depicted in Fig. 1c, works both as a computational base station and as a launch station for the satellites, relying either on an airbag-like or a cannon-like launching system. The swarm agents (Fig. 1d,e) are made to collide with the surface and acquire data, thus offering a good coverage of the object. A possible arrangement of sensors is shown in Fig. 1e, among which we find a magnetometer, an inertial measurement unit (IMU), and three cameras. A major part of our work is to provide a methodology to enable the swarm to be aware of their relative position; from the point of view of the swarm, this capability is called *proprioception*. As a case study, we consider exploring the comet 67P/Churyumov–Gerasimenko, which falls within the applicability limits of our approach. 67P is characterized by a large lobe ($4.1 \times 3.3 \times 1.8$ km) and a smaller one

($2.6 \times 2.3 \times 1.8$ km), connected by a "neck region". It has a mass of 9.982×10^{12} kg and a mean density of 0.533 g cm^{-3}.

The main contributions, with respect to the state-of-the-art, are as follows:

- Description and accuracy characterization of an algorithm for position determination of a swarm of agents in 3D knowing only the inter-agent distance, which can be subject to error;
- Demonstration of a lander-based launch of the swarm and SCB surface coverage;
- Application of the mascons approach to model the gravity field of comet 67P and characterization;
- Optimization-based approach for surface targeting in highly irregular gravity fields;
- Optimization-based approach for the discovery of long-duration orbits in highly irregular gravity fields;

In particular, the position determination algorithm is novel, and it stems as an extension of the known algorithm developed by Moore et al. in 2004 [16].

The paper is structured as follows: in Section 2 we explore in detail the literature relevant to our research. In Section 3, we describe the methodology, including the modelization of the gravity field, the dynamics, and the collision detection and localization algorithms; in Section 4 we present the results of a set of simulated scenarios, with emphasis on the quantification of the effectiveness of the methodology; finally, in Section 5 we give a conclusion to our work, highlighting the achievements and outlining future steps in this research.

2. Related works and mission overview

Historically, the first approach towards asteroids and comets was that of ground-based exploration through the use of telescopes [4]. As shown in Table 1, missions to SCB can be classified into five types: flyby, orbiter, impactor, lander, and sample return [6]. Additional

Table 1
Missions to small celestial bodies throughout the years 1978-present, with the addition of planned missions. The table shows only past missions which reached at least one objective.
* Scheduled or planned missions. †Failed objectives.

Mission	Operator	Launch–arrival	Small celestial body targets	Flyby	Orbiter	Impactor	Lander	Sample return
ICE	NASA/ESA	1978–85	21P/Giacobini–Zinner	✓				
			1P/Halley					
Vega 1&2	AH CCCP	1984–86	1P/Halley	✓				
Sakigake	ISAS	1985	1P/Halley	✓				
Giotto	ESA	1985–1986	1P/Halley	✓				
			26P/Grigg–Skjellerup (1992)					
Suisei	ISAS	1985–1986	1P/Halley	✓				
Galileo	NASA	1989–1993	951 Gaspra (1991)	✓				
			243 Ida (1993)					
NEAR Shoemaker	NASA	1996–2000	433 Eros	✓	✓		✓	
			253 Mathilde					
Deep Space 1	NASA	1998–2001	4015 Wilson–Harrington †	✓	✓		✓	
			9969 Braille (1999)					
			19P/Borrelly (2001)					
Stardust	NASA	1999–2004	81P/Wild	✓	✓		✓	✓
			5535 Annefrank (2002)					
Hayabusa	JAXA	2003–2005	25143 Itokawa		✓		✓	✓
Rosetta	ESA	2004–2014	67P/Churyumov–Gerasimenko	✓	✓		✓	
			2867 Šteins (2008)					
			21 Lutetia (2010)					
Deep Impact	NASA	2005–2005	9P/Tempel	✓				✓
			(163249) 2002 GT †					
New Horizons	NASA	2006–2015	134340 Pluto	✓				
			486958 Arrokoth (2019)					
Dawn	NASA	2007–2015	4 Vesta		✓			
			1 Ceres					
Chang'e-2	CNSA	2012	4179 Toutatis	✓				
Hayabusa2	JAXA	2014–2031*	162173 Ryugu	✓	✓	✓	✓	✓
			1998 KY$_{26}$ (2031*)					
OSIRIS-REx	NASA	2016–2018	101955 Bennu	✓	✓		✓	✓
Lucy	NASA	2021–2033*	152830 Dinkinesh (2023)	✓				
			52246 Donaldjohanson (2025)					
			3548 Eurybates (2027)					
			15094 Polymele (2027)					
			11351 Leucus (2028)					
			21900 Orus (2028)					
			617 Patroclus–Menoetius (2033)					
DART	NASA	2021–2022	65803 Didymos	✓		✓		
			(65803) Didymos I					
Psyche	NASA	2023*–2030*	16 Psyche		✓			
Hera	ESA	2024*–2026*	65803 Didymos		✓		✓	
DESTINY+	JAXA	2024*	3200 Phaethon	✓				
Tianwen-2	CNSA	2025*	469219 Kamo'oalewa	✓	✓		✓	✓
			311P/PANSTARRS					

classes would be human exploration and possibly settlement, but no instances of these exist to date. We can split them into two main categories: *remote* (flyby, orbiters) and *in-situ sensing* (lander, sample return), where impactors are left out, being a passive tool that does not provide data directly. Remote sensing has been used to glean information on the magnetic (e.g. Rosetta [1]), electric (e.g. Rosetta [17]) and gravitational field (e.g. Hayabusa 2 [2]) of SCBs. Furthermore, it was used to map their geometry, topography, and structure (e.g. Rosetta [5], Dawn [7]), as well as the type of regolith found on their surface (e.g. Hayabusa 2 [18]) and its chemical and mineralogical composition (e.g. NEAR Shoemaker [19], OSIRIS-REx [20], Dawn [7]). Regarding sample return, Zhang et al. in 2022 review the main methodologies in use and that are being studied [3].

2.1. Gravity field models

When dealing with SCB, one of the most immediate challenges is the geometry of the gravity field; since most of these objects have irregular shape, the resulting field influences the orbits, which tend to become chaotic [21]. In 2013, Melman et al. proposed a methodology to account for the state propagation of orbits in highly irregular gravity fields, and to evaluate the influence of limited knowledge of its characteristics [22]. In 2023, Li et al. show that the field can be mapped using the measure of the inter-satellite range between a main spacecraft and a small number of other deputies [23]. Park et al. show a method to compute the internal density of SCB using the navigation data from a spacecraft [24].

The most common approaches for representing the gravity field of an irregularly shaped body are briefly presented here. The most classical approach uses spherical harmonics to model the gravitational potential. This method usually lacks accuracy near the surface and might suffer convergence problems. Mascons models are a relatively simple approach, where a set of point masses (mass concentrations — *mascons*) are adopted to reproduce the body mass distribution [25]. The polyhedrons approach, firstly introduced by Werner et al. [26], approximates the body shape with an arbitrary polyhedron whose exact gravity field can be computed analytically. This is the most accurate method among the three, although it is more computationally expensive. In 2010, Zhang et al. showed the application of the polyhedron model for 433 Eros [27], whereas Wang et al. used the same method to analyze equilibrium points within the gravity fields of various small bodies [21]. In 2023, Wen et al. adopted a finite element method (FEM) to model the gravitational field of asteroid Arrokoth and compute its equilibrium points under three different heterogeneous internal structures hypothesis [28].

2.2. Monolithic versus swarm-based exploration

Contrary to the traditional approach to exploration, where a single monolithic probe is sent out to carry out operations on the surface or around it, another way has been proposed in the past and continues to be at the boundary of current missions: multi-agent systems [29], or swarms [30]. The case for these is that, in the case of space exploration, it may be beneficial to have redundant, distributed, and low-cost systems that are, however, less capable individually than a single, more complex, machine.

Surface robot swarms (termed nanorovers) have been proposed for the exploration of Mars [31], the Moon [32], and their settlement [33]. Carpentiero et al. proposed cooperating rovers forming a swarm built around autonomous guidance and vision-based navigation, to be used for planetary exploration [34]. Innovative architectures propose hopping robots [35,36], which have shown value in recent missions, e.g. DLR and CNES's MASCOT [37], and which promise good implementations of the swarm paradigm, i.e. lightweight, simple, small agents.

A somewhat simpler approach than that of nanorovers involves the use of nano-landers or small "impactors", i.e. agents designed to survive high-velocity landings from orbit, without propulsion. In 2017, Kalita et al. proposed a methodology to design such swarms using machine learning [38]. Ehrlich et al. discuss the DUSTEE project, which aims to use small trackers from a CubeSat deployer in orbit to explore wide lunar regions [39].

A good *corpus* of literature exists on using swarms to carry out the exploration of SCBs, an example of which is the work of Li et al. [23]. Ledbetter et al. proposed using a proper swarm of satellites to recover the density of the target SCB via measurements of its gravity field [40]. A key challenge in exploring SCBs is that of flying safely within a highly irregular gravity field, for which it may be beneficial to actively control the attitude of swarms [41–43]. Formation flying and reconfiguration have also been proposed for orbital construction [43].

Swarm flyby is an approach suitable when orbital insertion is not possible. Nallapu et al. present a framework to design spacecrafts and the related swarms and trajectories to enable flybys of planetary moons of designated areas [44,45]; the point is made that this might also be considered as a precursor for larger missions [42].

Finally, the concept of ChipSats emerges: gram-scale spacecrafts that can be deployed in large numbers to provide distributed sensing and communications on celestial targets [46]; these can be controlled via statistical approaches, as shown by Manchester and Peck in 2011 [47]. Their dynamics have been shown around irregular objects [48], but their case has been made for the exploration of the Moon as well [49]. Swarm control methodologies have been proposed, such as using magnetorquers [50].

Possible sensing aboard swarm satellites can be for the detection of micro-meteoroids, radiation, dust, and gas, as well as seismology [49]. Swarms have been proposed for mining [33] and for in-situ resources utilization (ISRU) [30].

2.3. Localization

The determination of the swarm agents' positions after their deployment, referred to as localization, is a major aspect of this work. Due to the lack of satellites for global positioning and to the impossibility of allocating beacon nodes in predetermined spots, the most suitable localization approach for SCB exploration relies on proximity-based methods. Neighborhood relationships, determined through range measurements, are used to estimate the nodes' reciprocal positions. This can be achieved for example through optical or radio inter-agent range measurements [51].

The localization problem is well known in the domain of wireless sensor networks (WSN) and, as such, many algorithms can be found in the literature. Savarese et al. [52] proposed the *Assumption*
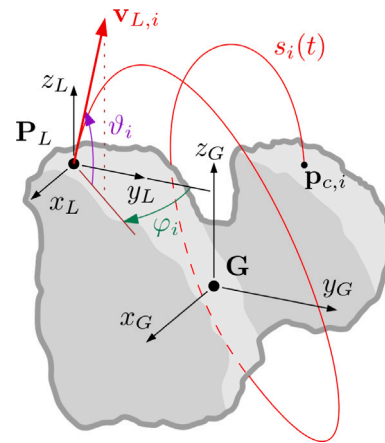

Fig. 2. Trajectory of a launched agent around a small celestial body.

Based Coordinates (ABC) algorithm, which relies on coordinates assumption and error compensation through redundant calculations and iterative refinements. The *Anchor-Free Localization* (AFL), proposed by Priyantha et al. in [53], uses a mass–spring optimization technique to correct localization errors starting from a "fold-free" nodes graph. Moore et al. [16] introduced the concept of robust quadrilaterals to avoid localization ambiguities in the presence of noise measurements.

2.4. Mission overview

In this section, we present the general outline of a possible mission to an SCB that implements and showcases the presented methodology.

The initial phase commences with the launch of the spacecraft and the attainment of the requisite interplanetary orbit towards the targeted SBC. Upon achieving the interplanetary orbit (i) the deep-space *coasting phase* begins, characterized by possible gravitational assists and maneuvers to refine the approach trajectory towards the target; (ii) orbit injection at the SBC. At this point, the *proximal phase* begins, consisting of (iii) the surface survey and gravimetric analysis of the SBC: potential landing sites compatible with agents launch are determined and the object's gravitational field is fine-tuned with local data. Next, the *descent and landing phase* follows, with the lander at the selected site on the celestial body. Immediately following this phase, the methodology proposed in this paper is framed.

Following landing, the *launch phase* begins: (1) the position of the base station is accurately determined; (2) the base station prepares for the launch of the agents; (3) the agents are launched. At this point, the *dissemination phase* sees all agents moving on suborbital trajectories while in constant communication with neighboring agents. This allows science data to be transferred to the base station for relay back to Earth, but, most importantly, the agents are localized using the approach described in this paper.

When agents start to collide with the surface of the SCB, the *end-of-mission phase* commences; (a) agents that are on the ground analyze the local features and relay data to other not-yet-landed agents that are passing overhead; (b) agents passing overhead relay data to the base station via other agents or directly, and provide the framework to fine-tune the localization of the agents on the ground; when most agents have collided with the surface, the possibility of assembling a network becomes limited, thus the mission ends.

3. Methodology

Referring to Fig. 2, we envision a launch platform located in $\mathbf{P}_L$ on the surface of the comet 67P/Churyumov–Gerasimenko, which we have elected as our case study. The center of mass $\mathbf{G}$ of the comet coincides
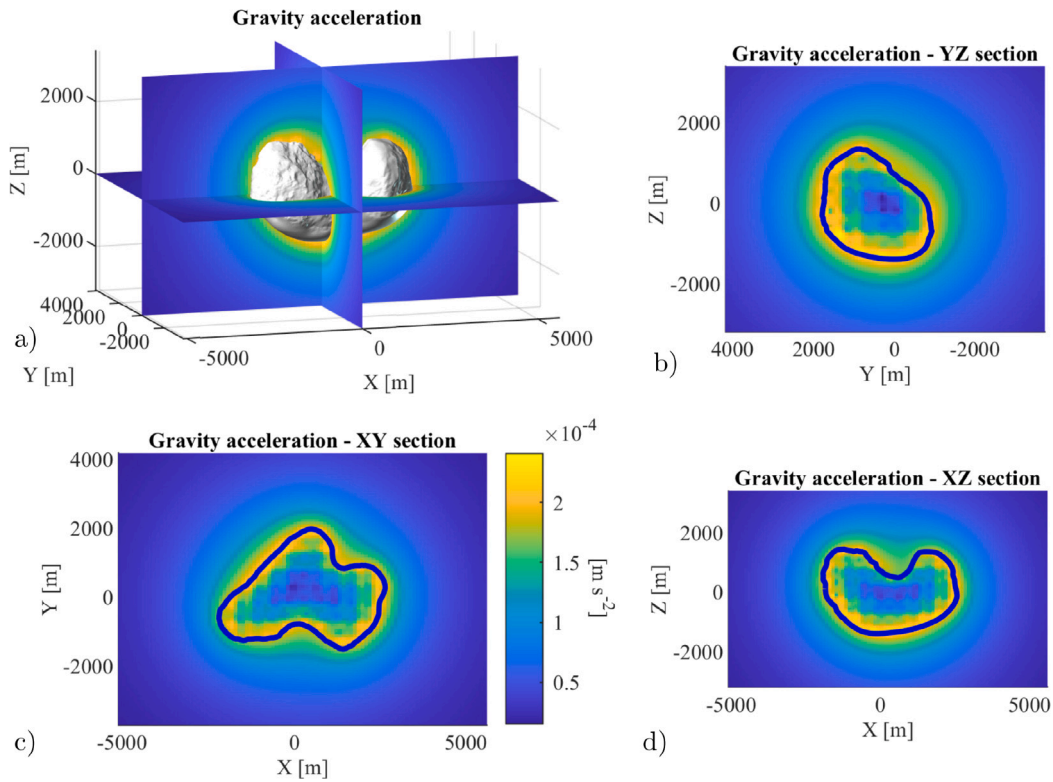
Fig. 3. Gravity field in terms of acceleration magnitude.

with its frame of reference (x_G, y_G, z_G). The platform, depicted in Fig. 1a–c launches agents along a trajectory $s(t)$, such that for each ith agent, an associated trajectory $s_i(t)$ can be determined. Ultimately, the trajectories terminate by colliding with the surface in point $\mathbf{p}_{c,i}$, where the agents are assumed to stop for the remaining time, i.e. no bouncing effects are considered in this work. Each agent is an active object with Radio Frequency (RF) connectivity and limited sensing capabilities. Most importantly, agents are capable of measuring their mutual distance via RF range-finding. In Fig. 1d, e we show a possible arrangement of sensors, among which we find a magnetometer, an inertial measurement unit (IMU), and three cameras. In this case study, each agent is 50 mm in diameter, while the entire lander has a footprint of approximately 1×1 m.

3.1. Gravitational field and voxelization

The comet's gravitational field has been modeled with a mascons approach, which uses a finite number of point masses (named mass concentrations or mascons) to reproduce the body's mass distribution. This choice has been made due to its lower computational cost with respect to the polyhedral method [28], even at cost of accuracy, while considering the already high cost of the localization algorithm.

The mascons topology has been determined by discretization of a volume containing the body in a set of m volumes. A cubic mesh was used, with the geometric center of each voxel placed on an ordered grid, while their centroids, not yet determined, will represent the mascons. These voxels are identified by their index $j = 1, \ldots, m$.

Each voxel was then divided into cubic sub-voxels in order to determine its mass and the position of its centroid. First, an occupancy ratio was assigned to each voxel and defined as follows,

$$O_r = \frac{n_{sv,int}}{n_{sv,tot}} ,$$ (1)

where $n_{sv,tot}$ represents the total number of its sub-voxels; while $n_{sv,int}$ the number of those contained in the comet volume. It follows that its

mass can be represented as

$$m_{v,j} = O_r \rho V ,$$ (2)

where ρ is the density of the voxel, assumed to be constant all over the comet and equal to $0.533\,\mathrm{g\,cm^{-3}}$, and V is its volume. The voxels that are fully outside of the comet will have a null occupancy ratio and mass, so they will not contribute to the body's gravitational field. The centroid of each voxel was then defined as the centroid of its sub-voxels inside the comet, or as its geometric center if it is completely outside the body. Fig. 3 shows the field topology adopted in the following simulations and obtained using mascons defined by voxels of dimension $1000 \times 1000 \times 1000$ m^3, each divided into 125 sub-voxels of dimension $200 \times 200 \times 200$ m^3; which results in 56 internal mascons.

The gravitational force exerted by the jth mascon on the ith orbiting agent can be expressed as follows,

$$\mathbf{F}_{i,j} = -\frac{Gm_{p,i}m_{v,j}}{\|\mathbf{r}_{i,j}\|^2} \hat{\mathbf{r}}_{i,j} ,$$ (3)

where G is the gravitational constant, $m_{p,i}$ and $m_{v,j}$ represent the ith agent and jth voxel masses respectively, $\mathbf{r}_{i,j}$ is the distance between the two objects and $\hat{\mathbf{r}}_{i,j}$ is its direction, defined as pointing to the agent. It follows that the total gravitational force exerted on the ith agent can be expressed as,

$$\mathbf{F}_i = \sum_{j=1}^{m} \mathbf{F}_{i,j} .$$ (4)

3.2. Dynamics model

Due to the irregular gravitational field of the comet, closed-form solutions for orbital mechanics are not available. The trajectory $s_i(t)$ traveled by the ith agent has been determined by using a first-order Euler integration scheme.

At each time-step, being $\mathbf{F}_{i,j}$ the gravitational force exerted by each jth mascon on the ith agent, we can introduce the dynamics of the
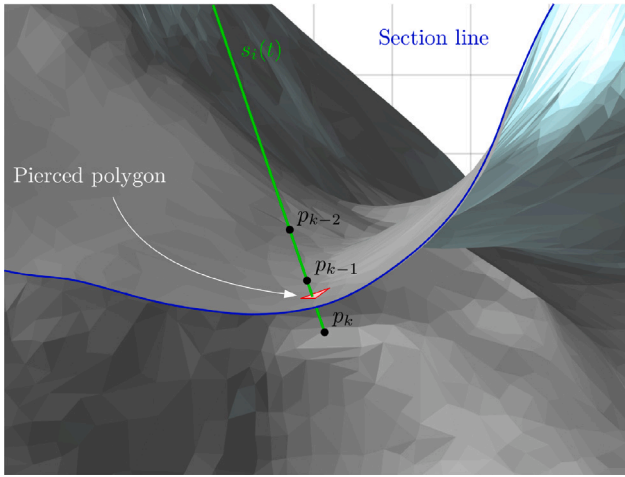
Fig. 4. Collision detection. In the figure, a section of the object surface mesh is shown. The section is solely for clarity. The trajectory is decomposed in successive positions $\mathbf{p}_k$; the pierced polygon is indicated in red. (For interpretation of the references to color in this figure legend, the reader is referred to the web version of this article.)

object in the following form,

$$m_p \ddot{\mathbf{x}}_i = \sum \mathbf{F}_{i,j} \tag{5}$$

by introducing the differential kinematics relation $\mathbf{u} = \dot{\mathbf{x}}$, it is possible to reduce (5) into state-space form, with structure as follows,

$$\mathbf{A}\dot{\mathbf{u}} = \mathbf{B} \tag{6}$$

This results in a first-order ODE which can be time-integrated. Within this study, we have elected to use Explicit Euler as the integration scheme:

$$\mathbf{u}(t_k) = \sum_{t=t_0}^{t_k} \mathbf{A}(t)^{-1} B(t)\delta t + \mathbf{u}(t_0). \tag{7}$$

The initial conditions for this integration are the launch parameters of the agent, given by the launch point $\mathbf{P}_L$, corresponding to the starting position, and its launch direction and velocity, corresponding respectively to the direction and magnitude of the initial velocity vector $\mathbf{v}_L$.

The trajectory $s_i(t)$ is then determined as the sequence of the positions traveled by the agent i between time t_0 and t_k.

3.3. Collision detection

To the extent of locating the landing point of an agent at the end of its trajectory $s_i(t)$ it is necessary to determine when and where it collides with the surface of the object. In this work, this is described by a surface mesh constituted of many triangular faces.

Beyond the collision between agents and surfaces, the possibility exists of collisions between individual agents. However, this paper operates under the assumption that these collisions are extremely unlikely. This assumption is supported by the observation that the likelihood of collision between agents is minimal from immediately after launch, considering the nature of the problem, i.e. that the agents are shot in opposite directions, their size is very small (≈ 5cm), and their orbits are many orders of magnitude larger (several km).

In order to keep the computational load under control, we only compute collision detection when an agent is close to the surface. If any mesh points within a threshold distance (assumed as twice the maximum length of the largest polygon of the surface mesh) are detected then the agent is considered to be close to the surface.

When this occurs, the trajectory $s_i(t)$ segment between its current kth and previous positions (segment $\mathbf{p}_k - \mathbf{p}_{k-1}$ in Fig. 4) is checked for

intersections with the surface mesh. A collision occurs if $\mathbf{p}_k$ and $\mathbf{p}_{k-1}$ are on opposite sides of the surface. Otherwise, if the segment does not intersect the mesh (case of positions $\mathbf{p}_{k-1}-\mathbf{p}_{k-2}$ in the same Figure), or if there are no mesh points within the threshold distance from the current position, then the agent has not collided yet. This process is repeated until the termination of the simulation or the detection of a collision. Once a collision occurs, the collision point $\mathbf{p}_{c,i}$ is determined as the intersection of the surface mesh with the previous-current positions segment, and the agent is assumed to be fixed in that point for the remaining simulation.

3.4. Localization

Perhaps the most important goal of this study is to determine the positions of the agents during flight. We assume that the agents are equipped with sensors able to measure their mutual distances without any directional information — this is called *inter-satellite link ranging* [23]. If we consider two generic agents 1 and 2, then the distance between them can be indicated as $l_{1,2}$. In more general terms, being $\lambda = [1, n]$ it follows,

$$\mathbf{l}_{i,\lambda} = \mathbf{q}_i - \mathbf{q}_\lambda . \tag{8}$$

By knowing the distances between agents in a group we can infer the structure of the group itself, i.e. the relative position between its members. We approached this problem using a three-dimensional extension of Moore's algorithm, which in fact shows that this is possible in two-dimensional space [16].

Where Moore's algorithm in the two-dimensional space considers planar graphs with *four* points (hence the name, quadrilaterals), we consider 3D objects with *five* points. A five-vertex graph is valid if it satisfies the following two conditions:

I. **Global rigidity** all ten distances between its nodes are known;
II. **Robustness** all of its five sub-tetrahedrons are robust. A tetrahedron is defined robust if it satisfies the equation,

$$b \sin^2(\theta) > d_{min} \tag{9}$$

where b is the length of its shortest height, θ is its smallest angle opposite to a height (see θ_A, θ_B, θ_C for the height of D in Fig. 5b) and d_{min} is a threshold determined based on the measurement noise.

Under these conditions, the nodes of such a graph can be localized relative to each other. However, it must be pointed out that, similarly to the two-dimensional case, the algorithm does not differentiate between a graph and its reflection. By looking at Fig. 5c, one may notice that we can define two possible reference frames (x, y, z) and (x', y', z') which describe a right- and a left-handed frame of reference respectively. It is important to note that the "correct frame" cannot be determined at this stage. Instead, our approach is that of considering both as candidates until the very end, where the base station will be able to differentiate the correct side.

Once two or more graphs (and their reflections) have been detected, then a pentalateral can be "chained" to another as long as they have four common nodes — these nodes define a common tetrahedron. If this succeeds, then, the fifth vertex can be localized by quadrilateration starting from its four known vertices. This process can be appreciated qualitatively in Fig. 5d.

For clarity, a *node neighbor* is defined as a (different) node that has bidirectional communications with it, i.e. it is in communication range and their mutual distance can be measured (and will be considered known). A *cluster* is defined as the subset composed of a central node and its neighbors.

The process by which the points $\mathbf{q}_i$ are localized can be divided into a local and global phase. Each of these can then be divided further. A summary of this structure is as follows:
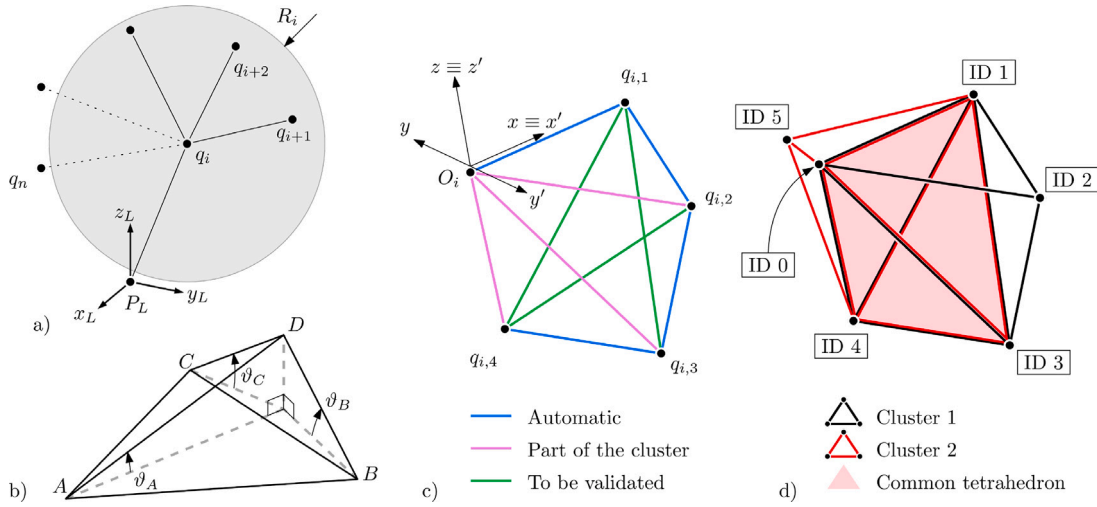
Fig. 5. Clustering and localization. (For interpretation of the references to color in this figure legend, the reader is referred to the web version of this article.)

A. *Local clusters definition*

i. **Clustering;** starting from each point $\mathbf{q}_i$, clusters are determined by taking the neighbors within line-of-sight and distance $l_{i,\lambda} \leq R_i$,

ii. **Search for pentalaterals;** points in each cluster are searched for all pentalaterals, following the procedure outlined in Fig. 5c,

iii. **Robustness screening;** non-robust pentalaterals are discarded,

iv. **Local quadrilateration;** points in each cluster are localized in the cluster local frame of reference using multilateration starting from each robust pentalateral; this creates a local map of each cluster,

B. *Global map assembly*

i. **Cluster stitching;** starting from the base station – whose location is known – each cluster is stitched to its neighbors; this creates the global map of the point cloud.

ii. **Mirror ambiguity resolution;** by localizing three or more agents from the base station the correct representation is selected.

The positions of the agents not localized after this process are finally determined by quadrilateration starting from the positions of their known neighbor nodes.

3.4.1. Local clusters definition

The general node $\mathbf{q}_i$ becomes the origin $\mathbf{O}_i$ of cluster C_i. The distances $l_{i,\lambda}$ between node $\mathbf{q}_i$ and node $\mathbf{q}_{i,\lambda} \in C_i$ are transmitted to the cluster origin node $\mathbf{O}_i$. Additionally, each node $\mathbf{q}_{i,\lambda} \in C_i$ broadcasts all of its own connections (and distances).

Referring to Fig. 5c, we can see that each pentalateral is built starting from $\mathbf{O}_i$ and finding four points $\mathbf{q}_{i,[1,\ldots,4]} \in C_i$. These are automatically part of the (possible) pentalateral because they are each connected to each other in a chain (blue links), and are also part of the cluster by definition (magenta links). At this point, the pentalateral is fully formed if the remaining connections exist (green links).

Finally, all pentalaterals in the cluster C_i are checked for robustness based on Eq. (9).

This entire process is detailed formally in Algorithm 1.

3.4.2. Local quadrilateration

Once the clusters are determined and the robustness of pentalaterals within them is established, we can determine the location of their

nodes using multilateration. In fact, only the ten distances between nodes are known at this point. We define the frame of reference of the pentalateral as such:

– The origin of the reference frame is $\mathbf{O}_i \equiv \mathbf{q}_{i,0}$,
– The x-axis is defined as the unit vector parallel to $\mathbf{q}_{i,1} - \mathbf{q}_{i,0}$,
– The y-axis lies in the plane defined by $\mathbf{q}_{i,0}$, $\mathbf{q}_{i,1}$ and $\mathbf{q}_{i,2}$,
– The z-axis completes a right-hand-side frame.

In parallel, we define a left-hand-side frame (x', y', z') where $x = x'$, $y = -y'$ and $z = z'$. This accounts for the reflection ambiguity.

The first two points can be defined easily, as such,

$$\mathbf{q}_{i,0} = \mathbf{O}_i = \{0,\, 0,\, 0\}, \quad \mathbf{q}_{i,1} = \{l_{0,1},\, 0,\, 0\}. \tag{10}$$

The third point can be defined from the distances between these three points;

$$\mathbf{q}_{i,2} = \left\{ \alpha l_{0,2},\ l_{0,2}\sqrt{1-\alpha^2},\ 0 \right\} \tag{11}$$

with $\alpha = \dfrac{l_{0,1}^2 + l_{0,2}^2 - l_{1,2}^2}{2 l_{0,1} l_{0,2}}$.

Note that in this case two points are actually defined, one in (x, y, z) and the other in (x', y', z') — its reflection.

The fourth point can be found using the same procedure used for $\mathbf{q}_{i,2}$; this generates yet another reflection ambiguity. Yet, only in this case, if we call these points $\mathbf{q}_{i,3,1}$ and $\mathbf{q}_{i,3,2}$, we can write,

$$\mathbf{q}_{i,3} = \begin{cases} \mathbf{q}_{i,3,1} & \text{if } \|\mathbf{q}_{i,0} - \mathbf{q}_{i,3,1}\| = l_{0,3} \\ \mathbf{q}_{i,3,2} & \text{if } \|\mathbf{q}_{i,0} - \mathbf{q}_{i,3,2}\| = l_{0,3} \end{cases}, \tag{12}$$

which allows us to solve this ambiguity.

The fifth point $\mathbf{q}_{i,4}$ can be found in the same way. In the end, we are left with two symmetric representations of the pentalateral – one in (x, y, z) and one in (x', y', z') – which both satisfy the set of distances.

The cluster local coordinate system is determined starting from one of the five-vertex robust graphs, chosen arbitrarily. Then, as many nodes as possible are localized by "chaining" the other robust pentalaterals to it. This process is repeated starting from a number of different graphs, thus creating several possible cluster map candidates; finally, the candidate that localized the most nodes is kept as the cluster map. This is shown in detail in Algorithm 2.

3.4.3. Cluster stitching and mirror ambiguity resolution

The last phase aims to create the global map of the network starting from the previously determined local maps. The coordinate system (x_L, y_L, z_L) of the launch station has been chosen as the global frame.
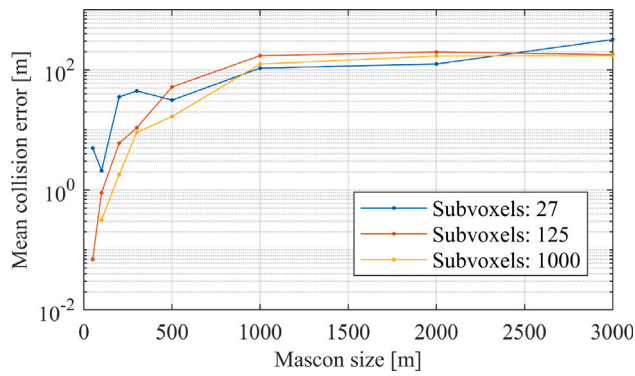
Algorithm 1 The first node of each graph is the central one, identified by q_i (Fig. 5a). The other four nodes, $q_{i,1} \dots q_{i,4}$, are selected between the neighbors of their previous one . The robust graphs are saved in the matrix **Q** as quintuplets of their nodes.

> **for all** neighbors $q_{i,1}$ of the central node q_i **do**
>> **for all** neighbors $q_{i,2}$ of the node $q_{i,1}$ **do**
>>> **for all** neighbors $q_{i,3}$ of the node $q_{i,2}$ **do**
>>>> **if** $q_{i,3}$ is neighbor of $q_{i,1}$ **then**
>>>>> **for all** neighbors $q_{i,4}$ of the node $q_{i,3}$ **do**
>>>>>> **if** $q_{i,4}$ is neighbor of the nodes $q_{i,1}$ **and** $q_{i,2}$ **then**
>>>>>>> **if** the conditions in Eq. (9) are verified **then**
>>>>>>>> Add the graph to **Q**.

Algorithm 2 The nodes within each pentalateral in **Q** are located. Pentalaterals are chained together to form a map of the cluster. The coordinates of the localized nodes are finally saved in the $\mathbf{L}_{best}$ matrix.

> **for all** graphs in **Q** do
>> Localize nodes in the considered pentalateral using multilateration (see Section 3.4.2),
>> Add the localized nodes to **L**,
>> $\mathbf{Q}_{aux} = \mathbf{Q}$,   ▷ *auxiliary matrix*
>> **while** other nodes are added to **L** do
>>> $c = 1$ ▷ *counter*
>>> **while** c is less than the graphs in $\mathbf{Q}_{aux}$ **do**
>>>> **if** the c-th graph of $\mathbf{Q}_{aux}$ has 4 nodes in common with **L**, **then**
>>>>> Localize the fifth node by quadrilateration from the other four,
>>>>> Add the node to **L**,
>>>>> Remove the graph from $\mathbf{Q}_{aux}$,
>>>> **else if** the graph has 5 common nodes with **L** **then**
>>>>> Remove the graph from $\mathbf{Q}_{aux}$,
>>>> **else**
>>>>> $c = c + 1$,
>> **if** **L** has more nodes than $\mathbf{L}_{best}$ **then**
>>> $\mathbf{L}_{best} = \mathbf{L}$,
>> **if** all the cluster nodes are in $\mathbf{L}_{best}$ **then**
>>> terminate the function.

Similarly to the process by which clusters are assembled starting from robust pentalaterals, the global map is built by finding common nodes between available clusters. However, it is important to recall that at this point each cluster still carries a mirror ambiguity. In principle, there exist two approaches to this particular part of the problem:

  i. Build two separate versions of the global map – one the mirror image of the other – and solve the mirror ambiguity at the end, thus discarding the incorrect global map version;
  ii. Solve the ambiguity for at least one cluster, and then assemble the rest of the clusters by solving the ambiguity for each of these.

In this instance, we have elected to follow the former. In fact, once the twin global maps have been assembled from the clusters, the launch station locates at least four points of the cloud in absolute terms. This can be achieved using directional RF range-finding, RF triangulation, or other similar techniques. The selected points should constitute a robust tetrahedron, following Eq. (9) to avoid yet other ambiguities. At this point, the correct global map is selected, based on the compatibility of the real locations of these points and their relative positions within the map.

The best rotation and translation are computed through a closed-form solution to the least-squares problem for the common nodes [54].

Using unit quaternions, the rotation problem is reduced to an eigenvalue-eigenvector problem. Let us call "old" the system already added to the global map and "new" the new candidate, and let $\mathbf{r}_{old,i}$ and $\mathbf{r}_{new,i}$ be the vectors identifying the common nodes in the old and new systems respectively, with $i = 1 \dots n$, where n is the number of common nodes. The centroids of the common nodes for the two systems can be defined as:

$$\bar{\mathbf{r}}_{new} = \frac{1}{n} \sum_{i=1}^{n} \mathbf{r}_{new,i}, \quad \bar{\mathbf{r}}_{old} = \frac{1}{n} \sum_{i=1}^{n} \mathbf{r}_{old,i}. \tag{13}$$

Considering that $\mathbf{r}'_{new,i} = \mathbf{r}_{new,i} - \bar{\mathbf{r}}_{old}$ and that $\mathbf{r}'_{old,i} = \mathbf{r}_{old,i} - \bar{\mathbf{r}}_{old}$, we can write,

$$\sum_{i=1}^{n} \mathbf{r}'_{new,i} \mathbf{r}'^{T}_{old,i} = \begin{bmatrix} S_{xx} & S_{xy} & S_{xz} \\ S_{yx} & S_{yy} & S_{yz} \\ S_{zx} & S_{zy} & S_{zz} \end{bmatrix} \tag{14}$$

The unit quaternion – which can be represented in matricial form as **R** – representing the best rotation is the eigenvector associated to the most positive eigenvalue of the matrix N defined as follows,

$$N = \begin{bmatrix} S_{xx} + S_{yy} + S_{zz} & S_{yz} - S_{zy} \\ S_{yz} - S_{zy} & S_{xx} - S_{yy} - S_{zz} \\ S_{zx} - S_{xz} & S_{xy} + S_{yx} \\ S_{xy} - S_{yx} & S_{zx} + S_{xz} \\ \\ S_{zx} - S_{xz} & S_{xy} - S_{yx} \\ S_{xy} + S_{yx} & S_{zx} + S_{xz} \\ -S_{xx} + S_{yy} - S_{zz} & S_{yz} + S_{zy} \\ S_{yz} + S_{zy} & -S_{xx} - S_{yy} + S_{zz} \end{bmatrix} \tag{15}$$

Finally, the best translation is then computed as follows,

$$\mathbf{r}_0 = \bar{\mathbf{r}}_{old} - \mathbf{R} \bar{\mathbf{r}}_{new}. \tag{16}$$

3.5. Validation of the mascons model

In order for the mascons-based discretization approach to be considered realistic, it is important to validate it with regard to our specific needs. To this extent, we performed a study on the discretization convergence considering both the voxel and sub-voxel subdivisions outlined in 3.1. Results are shown in Fig. 6.

4. Results and discussion

In this section we show the results of a set of scenarios. In particular, we show two ways in which the trajectories of launched agents can be shaped, in order to fulfill specific objectives. In the former, we show the targeting of a landing point using optimization techniques; in the latter, we show how a similar approach can be used to maximize flight time. Next, we show a quantitative analysis of the surface coverage that can be achieved using this swarm approach. Finally, we take advantage of an integrated simulation to characterize the localization error of the swarm agents during flight and at landing.

4.1. Targeting of a landing point

Objective of this section is to determine whether it is possible to find the launch parameters such that an agent lands in a predetermined desired point of the surface.

The launch parameters evaluated in this study are the following three:

  – Azimuth $\varphi \in [0, 2\pi]$ rad. See Fig. 2;
  – Elevation $\vartheta \in [0, \pi/2]$ rad;
  – Velocity $\mathbf{v}_{L,i}$ with $\|\mathbf{v}_{L,i}\| = v_{L,i} \in [0, 1]$ m s^{-1}.

The results of a *Design of Experiments* (DOE) obtained by discretizing its launch parameters and illustrated in Fig. 7(a), show that the obtained landing points are distributed over most of the surface. Hence – at least from this launch position – we show that it is possible to target a landing point in any location of the asteroid.

An optimization was then performed for each of sixty different target points chosen randomly. The optimized parameters were the launch parameters ϑ_i, φ_i, and $v_{L,i}$, while the optimization objective was to minimize the distance between the desired target point and the actual

Fig. 6. Discretization convergence. The relation between the mean collision error and the mascon size is shown here. Three different sub-voxelizations are shown.

landing point. The chosen optimization algorithm was a SIMPLEX with 500 iterations. The launch parameters domain was restricted for each target point according to the values that, in the previous DOE, gave a landing point in its proximity. This way, we prevented the SIMPLEX algorithm from falling in some local minima of the objective function.

The error distribution between the obtained and the desired landing point for all the sixty target points is reported in Fig. 7(c). This result shows that for each of them, it has been possible to find some launch parameters such that an agent can land on the target point with an error less that 1 mm.

4.2. Flight time maximization

During the simulations it occurred that the majority of the agents could not be localized in the final part of their trajectories due to the gradual loss of connections in the network. This brought the need to launch some agents with trajectories stable enough that, while orbiting, they would increase the connectivity and help with these localizations.

To determine such trajectories, another launch parameters optimization as been executed. The optimization objective was to maximize the flight time of a trajectory, with the restriction that it must remain in proximity of the asteroid in order to keep the connections with the other agents.

Many launch parameters have been found such that the associated trajectories orbit the body for hundreds of hours, enough to help with the localization of the previously landed agents.

Fig. 7(b) shows the example of a 72 h long trajectory obtained with this optimization approach.

4.3. Surface coverage analysis

This section evaluates the relation between the number of launched agents and the amount of asteroid surface covered by them.
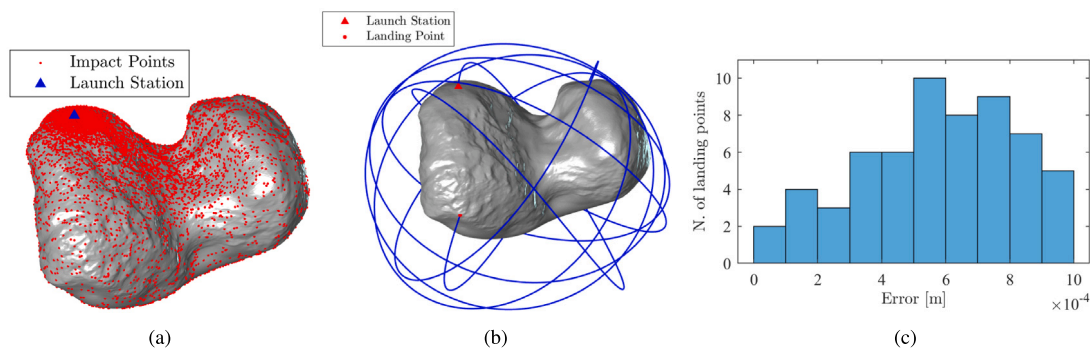
A triangular uniform meshed sphere has been used to divide the surface of the object into roughly equal area regions. This is achieved by projecting the mesh onto the object. The sphere was bigger than the asteroid and centered in its center of gravity so that the projections of the mesh triangles have been used to divide the asteroid surface.

An agent is considered to cover all the surface of the region it lands in, i.e. each agent will cover just one region, while a region can be covered by one or more agents.

The agents launch parameters have been taken randomly, while their number has been varied from 10 to 1000. Five simulations have been conducted for each value of the agents number due to the randomness of the launch parameters.

The coverage analysis results obtained for a sample simulation, using 1000 agents in the case of 320 surface divisions, are shown in Fig. 8. Specifically, in Fig. 8(a) the probability distribution is shown of the launch direction; the covered surface is depicted in Fig. 8(b).

The plot in Fig. 9(b) shows how the percentage of covered surface varies with the number of deployed agents. First, we can see that there is a growing trend, as could be expected, meaning that a bigger number of agents covers a bigger surface. We can also see that the coverage difference between a higher and a lower agent number becomes more marked when the number of surface divisions decreases (i.e. their dimension increases). This can be explained by the fact that a smaller region has a lesser impact on the overall covered surface so even a large number of them could add just some percentage points to it. On the other hand, even though there will probably be more agents covering the same areas, a single bigger region will have a greater impact on the overall coverage.

These results show the importance of balancing the number of deployed agents with their distribution and coverage capacities. Well-distributed agents with high coverage ranges could cover a major part of the surface, even with a not-so-large number of them.

4.4. Localized agents percentage

This section aims to determine how the percentage of localized agents depends on the number of agents in the swarm.

The agents have been deployed with random launch directions and velocities, while their number has been varied from 10 to 70. Six simulations have been run for each value of the agents number in order to rely on more datasets due to the randomness of the launch parameters.

The evolution of the localized agents percentage is represented in Fig. 9(a).

The results show a growing trend of the localization percentage with respect to the number of deployed agents, according to the higher connectivity of the network. They also show that, regardless of the number of agents, this percentage drops to zero quite quickly due to the gradual loss of connections caused by the distancing of the agents from each other and from the base station.
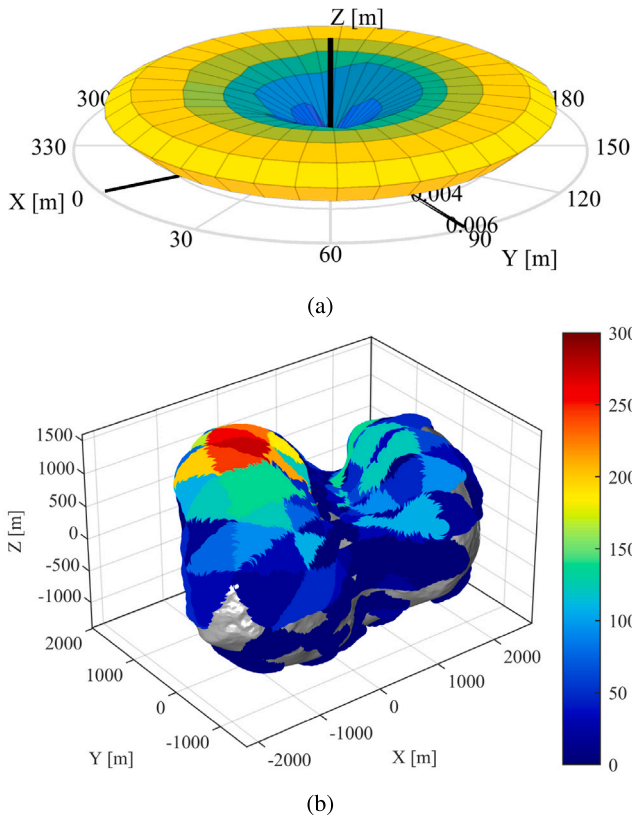

(a)   (b)   (c)

Fig. 7. Simulation examples. (a) Landing points of approximately 8000 objects launched in the DOE. (b) Example of a long-duration orbit. (c) Landing error distribution compared to intended targets.

(a)

(b)

Fig. 8. Launch of 1000 agents. (a) Launch direction distribution in terms of probability; (b) Coverage of the surface.

4.5. Integrated simulation and error characterization

In order to bring together all aspects discussed in the previous sections, a simulation was executed that integrates the dynamic and the gravity field models, collision detection, and localization algorithms. This allows us to evaluate the localization effectiveness and accuracy in a realistic scenario.
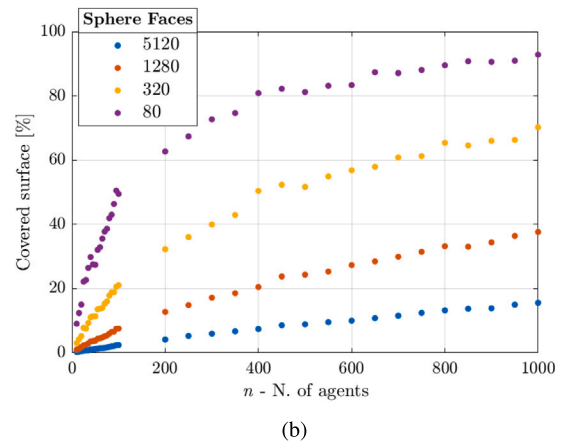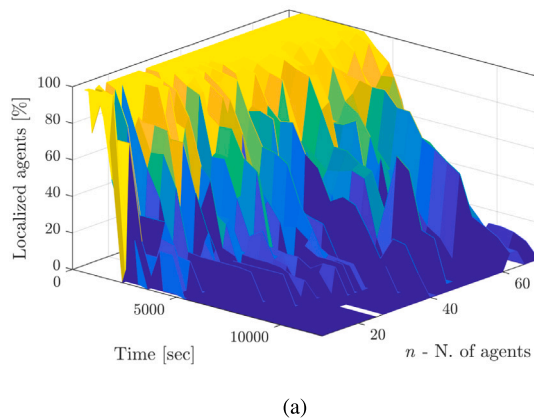
Within this simulation a number of 65 agents were launched. Specifically, 41 of them, which we will refer to as "first group" of agents, were intended to land in predetermined points, so their launch parameters have been chosen from the optimization results in Section 4.1, while the other 24, the "second group" of agents, have been chosen between the long time trajectories resulting by Section 4.2 in order to increase the connectivity of the network.

It is worth specifying that, while the agents of the second group have been specifically selected to ensure an high connectivity of the network all around the body, the first group agents landing points were chosen randomly (as mentioned in Section 4.1), i.e. they are representative of a generic "first group" of agents. No distribution strategies have been adopted for them yet, even thought their study would be a worthy subject for future researches. Various aspects can be of interest, e.g. homogeneous surface coverage, optimized accuracy distribution, time-effectiveness etc. Works like [55], where Wen et al. studied the SCBs reachable domain when hopping from their surface, could be helpful for such a study.

A uniform random error in the range $\varepsilon = [-1, 1]$m has been applied to each distance measured between the nodes in order to simulate the presence of measurement noise. The probability distribution $f(\varepsilon)$ thus can be written as follows,

$$f(\varepsilon) = \begin{cases} 1/2 & for \ -1 \le \varepsilon \le 1 \\ 0 & for \ \varepsilon < -1 \ or \ \varepsilon > 1 \end{cases}. \tag{17}$$

Fig. 10(a) shows the time evolution of the number of localized agents. The blue line refers to all the 65 agents, while the red one only considers the first group of them, which is the most interesting to be localized.

Three main time ranges can be identified:

0 s to 0.4×10^5 s : all the launched agents are in flight. The blue curve has a first rise due to the launch delay applied to some of the second group agents. Both curves then decrease rapidly according to the progressive landing of the first group of agents.

0.4×10^5 s to 3.3×10^5 s : the agents of the first group have already collided with the surface. The localization percentage is still high, especially for the red curve, meaning that the second group of agents is able to localize the first landed group.

3.3×10^5 s to 1×10^6 s : all the agents are landed except for four agents of the second group that are still orbiting. There still are some periodic localizations according to these four agents flying in the vicinity of the base station.
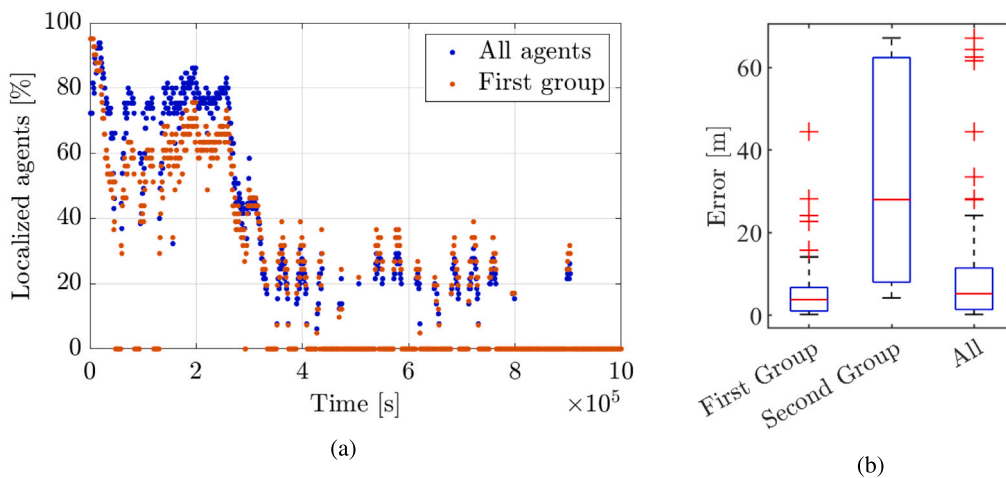

(a)

(b)

Fig. 9. Surface coverage and localization process characterization. (a) Localization as a function of n and time t; (b) Coverage of the surface as a function of the number n of agents.

Fig. 10. Complete simulation results: localization accuracy. (a) Localized agents as a function of time t; (b) Accuracy of localization at collision.

Regarding the precision of these localizations, we can distinguish the two cases of identifying an agent when it is still flying and identifying an agent after it has landed.

In the first case, each localization refers to a different point of the trajectory. Knowing the expected trajectories, the error of each estimated position can be calculated in reference to its expected counterpart. Then the outliers can be found and eliminated for each agent so that the remaining positions will give us our reconstruction of the trajectories.

After eliminating the outliers, defined as the values that are more than three scaled median absolute deviations (MAD) from the median, the remaining mean error of all the 65 agents is 8.5 m.

Fig. 10(b) shows the localization errors. We can see that there is a good precision for the first group of agents, with a mean error of 6.5 m. We can also identify some of the second group agents after they collided, although with less precision.

Fig. 11(a) shows the estimated positions (yellow) along the trajectories for the first group of agents, and their real counterparts (black). We can see that the curves are mostly overlapped; additionally, by looking at Fig. 11(b) we can appreciate that the localization error is comparably small for most of the trajectories. This means that we are able to carefully identify the agents along their flight path and to accurately assign accurate positions to readings performed by the sensors. The agents of the second group are not represented for clarity, due to their convoluted and long-period orbits.

In the case of identifying the collision point of an agent, instead, all the localizations made after its landing refer to the same position. In order to determine the collision point, we first calculated the centroid of its estimated positions, and then, referring to their distances from this centroid, the outliers have been eliminated. Finally, the landing point has been determined as the centroid of the remaining positions.

Fig. 11(c) reports a graphic representation of the simulation. We can see that the estimated and the real landing points are overlapped, meaning that the obtained precision enables the correct localization of the agents.

In order to better validate the localization accuracy and to characterize its surface distribution, about 420 additional simulations have been executed starting from the previous one. The first group agents' launch parameters have been randomly perturbed up to 15% of their values, allowing an overall spread distribution of impact points on the surface.

Fig. 12a and b show the estimated collision points for the first groups of agents of all the simulations (about 16600 agents), colored according to their error. We can clearly see that there is a zone, corresponding to the "neck region" of the comet, where the accuracy is higher, with most localization errors lower than 1 m. Outside this area the error increases until outlier values in the order of hundreds of meters. The reason for this distribution is the position of the launch station. The neck region is relatively close and within line-of-sight and, as such, it is easier for a second group of agents to create a chain of robust pentalaterals connecting it to the base station. In contrast, the hidden zones have fewer localizations available for estimating their collision points. Fig. 12c and d divide the surface into 1280 regions, similarly to Section 4.3, and color them according to the average localization error among the agents landed in each one (note its logarithmic scale). The gray zones have not been reached in these simulations.

The overall localization errors after a collision are represented in Fig. 13 for the agents of the first groups (about 16600 agents) and the collided ones of the second groups (about 4400 agents). The Y-axis represents the fraction of agents with an error lower than the associated X-value, e.g. 84% of the first group agents (red curve) are localized with an error less than 10 m.

5. Conclusion

In this work we have shown that a small celestial body can be explored by taking advantage of a swarm of small low-cost agents capable of performing inter-agent range measurements.

We have detailed a methodology to simulate the gravitational environment and the orbital dynamics around an irregularly shaped object like comet 67P/Churyumov–Gerasimenko. Special effort was devoted to the development of a series of algorithms to perform the localization of the swarm agents based on the distances between mutually in-range agents. The outcoming methodology allows the swarm to gain proprioception – the knowledge of the location of its parts – during flight and at the moment of landing. This enables, in principle, the up-close surveying of vast areas of the surface at a comparatively small cost and complexity increase.

We reported an in-depth characterization of the localization methodology, which gives insight into the capability of the swarm to perceive its geometry in space. Along with this, we presented a detailed
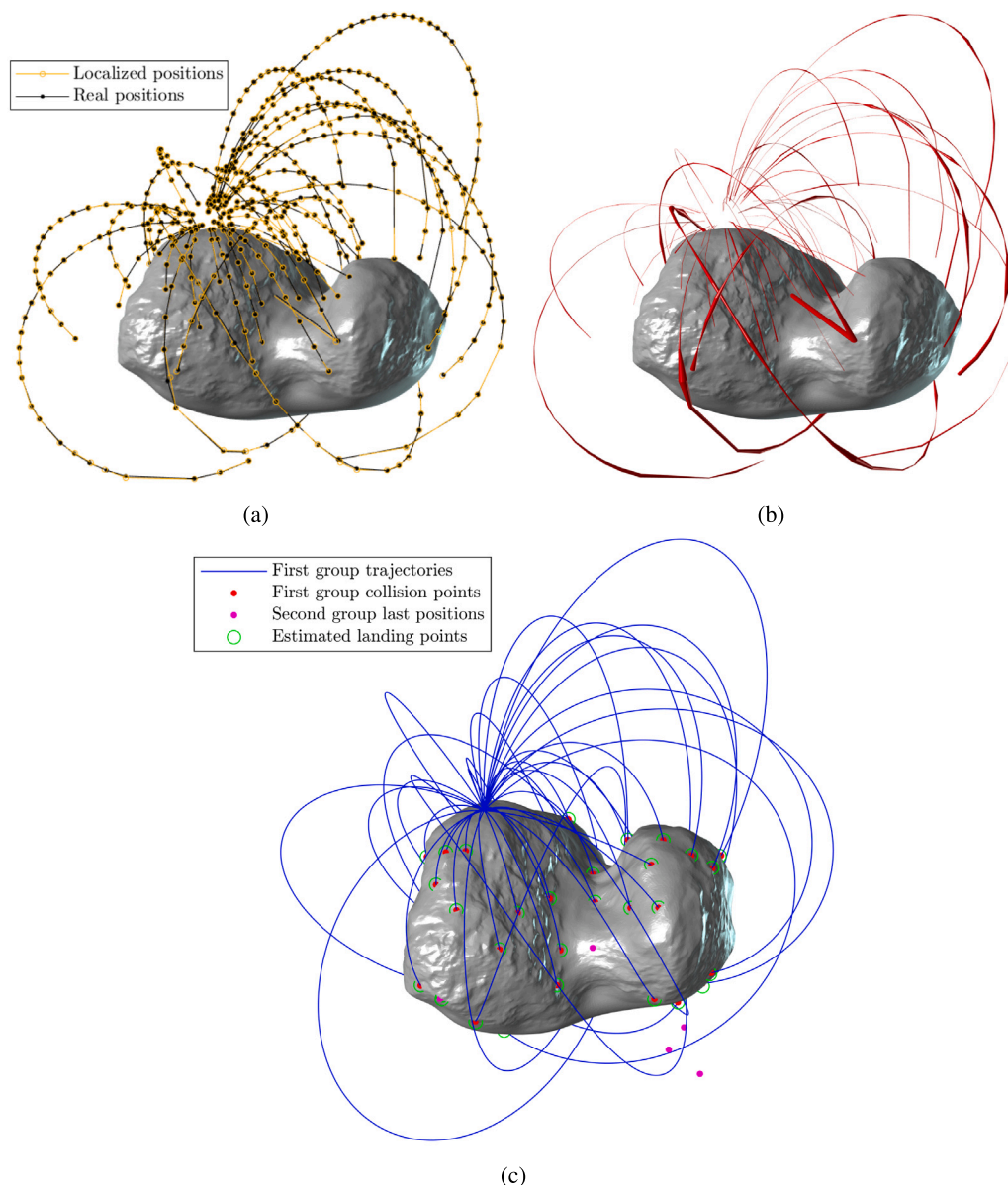
Fig. 11. Complete simulation results: trajectories. (a) Comparison between real and estimated trajectories; (b) Localization estimation errors along the trajectories. Here, the radius of the tube represents the localization error on a 1:1 scale. (c) Illustration of the complete (nominal) trajectories, showing nominal collision points compared to estimated collision locations. The four second-group objects (magenta) are still in flight. (For interpretation of the references to color in this figure legend, the reader is referred to the web version of this article.)

sensitivity analysis of localization deviations based on the range-finding measurement error; furthermore, we showed how the number of agents in the swarm impacts the surface coverage of the object. Finally, we demonstrated how having a subset of the agents following longer-period orbits positively impacts the localization of the grounded agents, leading to better performance.

In the future, we plan to validate the methodology in an experimental environment involving the launch of a small number of agents. Furthermore, more effort should be put into the development of scientific payloads targeted to this specific class of exploration scenario. Finally, in the event of a real mission, given the large number of agents that are to rest on the surface of small celestial bodies, more studies have to be carried out regarding the influence of these delicate extraterrestrial environments.

CRediT authorship contribution statement

Simone Cottiga: Investigation, Methodology, Software, Validation, Visualization, Writing – original draft, Writing – review & editing. **Matteo Caruso:** Methodology, Supervision, Writing – original draft, Writing – review & editing. **Paolo Gallina:** Conceptualization, Writing – original draft, Writing – review & editing. **Stefano Seriani:** Conceptualization, Funding acquisition, Methodology, Project administration, Supervision, Validation, Writing – original draft, Writing – review & editing.

Declaration of competing interest

The authors declare that they have no known competing financial interests or personal relationships that could have appeared to influence the work reported in this paper.
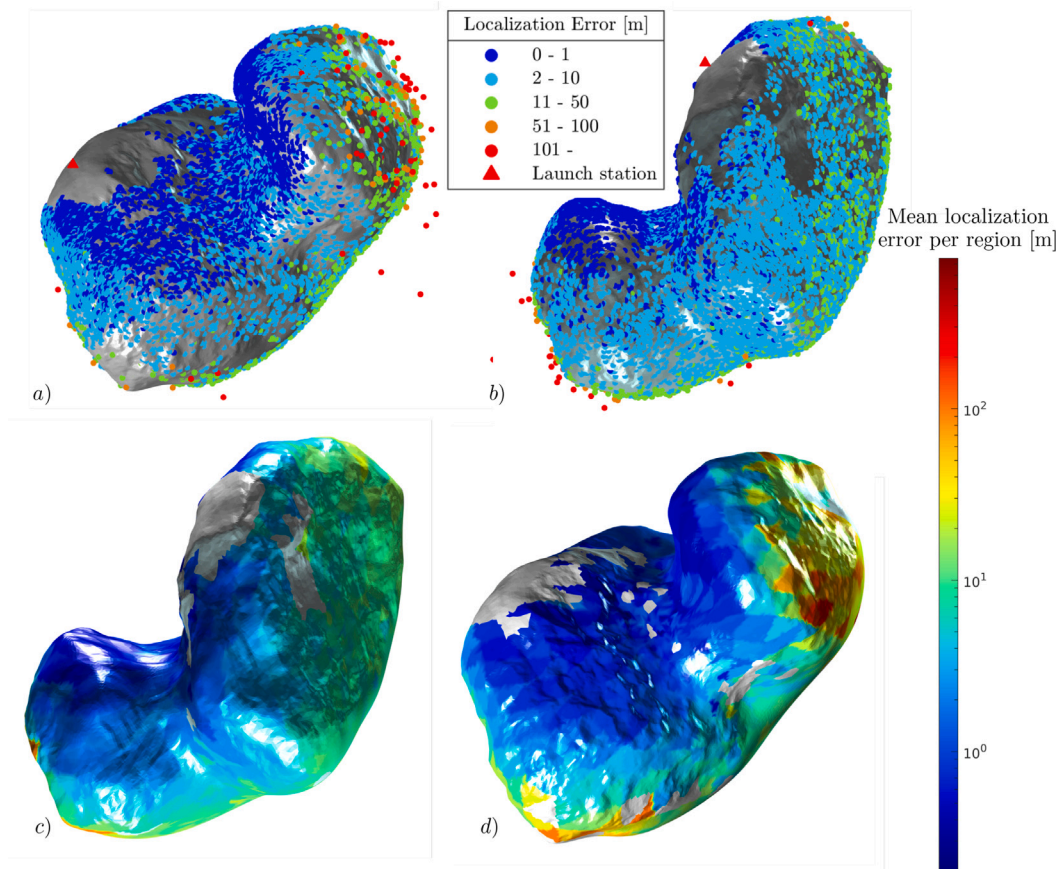
Fig. 12. Surface distribution of the first groups localization error after collision. Estimated collision points in front (a) and back (b) views. Surface divided in regions in back (c) and front (d) views.
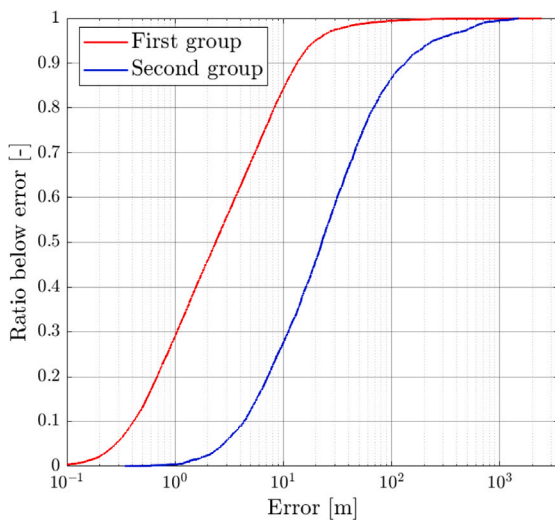

Fig. 13. Localization accuracy after collision of all the simulations.

References

[1] F. Plaschke, T. Karlsson, C. Götz, C. Möstl, I. Richter, M. Volwerk, A. Eriksson, E. Behar, R. Goldstein, First observations of magnetic holes deep within the coma of a comet, Astron. Astrophys. 618 (2018) http://dx.doi.org/10.1051/0004-6361/201833300, Cited by: 22; All Open Access, Green Open Access, Hybrid Gold Open Access. URL https://www.scopus.com/inward/record.uri?eid=2-s2.0-85056121056&doi=10.1051%2f0004-6361%2f201833300&partnerID=40&md5=9fad7f3e4dfa4c7be955c41823891b8b.

[2] S. Kikuchi, S.-i. Watanabe, T. Saiki, H. Yabuta, S. Sugita, T. Morota, N. Hirata, N. Hirata, T. Michikami, C. Honda, Y. Yokota, R. Honda, N. Sakatani, T. Okada, Y. Shimaki, K. Matsumoto, R. Noguchi, Y. Takei, F. Terui, N. Ogawa, K. Yoshikawa, G. Ono, Y. Mimasu, H. Sawada, H. Ikeda, C. Hirose, T. Takahashi, A. Fujii, T. Yamaguchi, Y. Ishihara, T. Nakamura, K. Kitazato, K. Wada, S. Tachibana, E. Tatsumi, M. Matsuoka, H. Senshu, S. Kameda, T. Kouyama, M. Yamada, K. Shirai, Y. Cho, K. Ogawa, Y. Yamamoto, A. Miura, T. Iwata, N. Namiki, M. Hayakawa, M. Abe, S. Tanaka, M. Yoshikawa, S. Nakazawa, Y. Tsuda, Hayabusa2 landing site selection: Surface topography of Ryugu and touchdown safety, Space Sci. Rev. 216 (7) (2020) http://dx.doi.org/10.1007/s11214-020-00737-z, Cited by: 16. URL https://www.scopus.com/inward/record.uri?eid=2-s2.0-85092545241&doi=10.1007%2fs11214-020-00737-z&partnerID=40&md5=69ee595b42cdaea0fe3821333f8d1407.

[3] X. Zhang, G. Zhang, H. Xie, M. Gao, Y. Wen, A review of sampling exploration and devices for extraterrestrial celestial bodies, Space Sci. Rev. 218 (8) (2022) http://dx.doi.org/10.1007/s11214-022-00926-y, URL https://www.scopus.com/inward/record.uri?eid=2-s2.0-85140237938&doi=10.1007%2fs11214-022-00926-y&partnerID=40&md5=1830b6651fc729e0e00e38cc5ad7c678.

[4] P. Vernazza, M. Ferrais, L. Jorda, J. Hanuš, B. Carry, M. Marsset, M. Brož, R. Fetick, M. Viikinkoski, F. Marchis, F. Vachier, A. Drouard, T. Fusco, M. Birlan, E. Podlewska-Gaca, N. Rambaux, M. Neveu, P. Bartczak, G. Dudziński, E. Jehin, P. Beck, J. Berthier, J. Castillo-Rogez, F. Cipriani, F. Colas, C. Dumas, J. Ďrech, J. Grice, M. Kaasalainen, A. Kryszczynska, P. Lamy, H. Le Coroller, A. Marciniak, T. Michalowski, P. Michel, T. Santana-Ros, P. Tanga, A. Vigan, O. Witasse, B. Yang, P. Antonini, M. Audejean, P. Aurard, R. Behrend, Z. Benkhaldoun, J. Bosch, A. Chapman, L. Dalmon, S. Fauvaud, H. Hamanowa, H. Hamanowa, J. His, A. Jones, D.-H. Kim, M.-J. Kim, J. Krajewski, O. Labrevoir, A. Leroy, F. Livet, D. Molina, R. Montaigut, J. Oey, N. Payre, V. Reddy, P. Sabin, A. Sanchez, L. Socha, VLT/SPHERE imaging survey of the largest main-belt asteroids: Final results and synthesis, Astron. Astrophys. 654 (2021) http://dx.doi.org/10.1051/0004-6361/202141781, Cited by: 36; All Open Access, Green Open Access, Hybrid Gold Open Access. URL https://www.scopus.com/inward/record.uri?eid=2-s2.0-85117069669&doi=10.1051%2f0004-6361%2f202141781&partnerID=40&md5=4c06f4b52939b2c3de1284e14be25ea1.

[5] P. Weissman, A. Morbidelli, B. Davidsson, J. Blum, Origin and evolution of cometary nuclei, Space Sci. Rev. 216 (1) (2020) http://dx.doi.org/10.

1007/s11214-019-0625-7, Cited by: 18. URL https://www.scopus.com/inward/record.uri?eid=2-s2.0-85077862577&doi=10.1007%2fs11214-019-0625-7&partnerID=40&md5=85a2d76cc3a1af8d2f0560f7b151e76e.

[6] M. Barucci, E. Dotto, A. Levasseur-Regourd, Space missions to small bodies: Asteroids and cometary nuclei, Astron. Astrophys. Rev. 19 (1) (2011) http://dx.doi.org/10.1007/s00159-011-0048-2, URL https://www.scopus.com/inward/record.uri?eid=2-s2.0-84884706521&doi=10.1007%2fs00159-011-0048-2&partnerID=40&md5=4ab91627706bfd147fb5d44c709231e7.

[7] T. Prettyman, N. Yamashita, M. Toplis, H. McSween, N. Schörghofer, S. Marchi, W. Feldman, J. Castillo-Rogez, O. Forni, D. Lawrence, E. Ammannito, B. Ehlmann, H. Sizemore, S. Joy, C. Polansky, M. Rayman, C. Raymond, C. Russell, Extensive water ice within ceres' aqueously altered regolith: Evidence from nuclear spectroscopy, Science 355 (6320) (2017) http://dx.doi.org/10.1126/science.aah6765, Cited by: 152. URL https://www.scopus.com/inward/record.uri?eid=2-s2.0-85006758512&doi=10.1126%2fscience.aah6765&partnerID=40&md5=f788e8c691e0ba036a4c9a439f1a2656.

[8] B.V. Sarli, Y. Tsuda, Hayabusa 2 extension plan: Asteroid selection and trajectory design, Acta Astronaut. 138 (2017) 225–232, http://dx.doi.org/10.1016/j.actaastro.2017.05.016, Cited by: 19. URL https://www.scopus.com/inward/record.uri?eid=2-s2.0-85020260047&doi=10.1016%2fj.actaastro.2017.05.016&partnerID=40&md5=99671d598e17b1c05e90717a6e052daa.

[9] S.A. Sandford, E.B. Bierhaus, P. Antreasian, J. Leonard, C.K. Materese, C.W. May, J.T. Songer, J.P. Dworkin, D.S. Lauretta, B. Rizk, Outgassing from the OSIRIS-REx sample return capsule: characterization and mitigation, Acta Astronaut. 166 (2020) 391–399, http://dx.doi.org/10.1016/j.actaastro.2019.07.043, Cited by: 7. URL https://www.scopus.com/inward/record.uri?eid=2-s2.0-85074281248&doi=10.1016%2fj.actaastro.2019.07.043&partnerID=40&md5=0efee88dbbd0240e3fa084a7d3698f82.

[10] A. Capannolo, G. Zanotti, M. Lavagna, E.M. Epifani, E. Dotto, V. Della Corte, I. Gai, M. Zannoni, M. Amoroso, S. Pirrotta, Challenges in LICIA cubesat trajectory design to support DART mission science, Acta Astronaut. 182 (2021) 208–218, http://dx.doi.org/10.1016/j.actaastro.2020.09.023, Cited by: 11; All Open Access, Green Open Access. URL https://www.scopus.com/inward/record.uri?eid=2-s2.0-85101123807&doi=10.1016%2fj.actaastro.2020.09.023&partnerID=40&md5=8504c34620be7562c2da4ad21c6837b0.

[11] C.B. Olkin, H.F. Levison, M. Vincent, K.S. Noll, J. Andrews, S. Gray, P. Good, S. Marchi, P. Christensen, D. Reuter, H. Weaver, M. Pätzold, J.F. Bell, V.E. Hamilton, N.D. Russo, A. Simon, M. Beasley, W. Grundy, C. Howett, J. Spencer, M. Ravine, M. Caplinger, Lucy mission to the trojan asteroids: Instrumentation and encounter concept of operations, Planet. Sci. J. 2 (5) (2021) http://dx.doi.org/10.3847/PSJ/abf83f, Cited by: 10; All Open Access, Gold Open Access, Green Open Access. URL https://www.scopus.com/inward/record.uri?eid=2-s2.0-85114715333&doi=10.3847%2fPSJ%2fabf83f&partnerID=40&md5=ee83655ffe09edb5ce317f0db5a3d576.

[12] W. Hart, G.M. Brown, S.M. Collins, M. De Soria-Santacruz Pich, P. Fieseler, D. Goebel, D. Marsh, D.Y. Oh, S. Snyder, N. Warner, G. Whiffen, L.T. Elkins-Tanton, J.F. Bell, D.J. Lawrence, P. Lord, Z. Pirkl, Overview of the spacecraft design for the psyche mission concept, in: IEEE Aerospace Conference Proceedings, 2018-March, 2018, pp. 1–20, http://dx.doi.org/10.1109/AERO.2018.8396444, Cited by: 35. URL https://www.scopus.com/inward/record.uri?eid=2-s2.0-85049830858&doi=10.1109%2fAERO.2018.8396444&partnerID=40&md5=4fc954917bf320378c9575b845e73873.

[13] P. Michel, M. Küppers, A.C. Bagatin, B. Carry, S. Charnoz, J. de Leon, A. Fitzsimmons, P. Gordo, S.F. Green, A. Hérique, M. Juzi, Ö. Karatekin, T. Kohout, M. Lazzarin, N. Murdoch, T. Okada, E. Palomba, P. Pravec, C. Snodgrass, P. Tortora, K. Tsiganis, S. Ulamec, J.-B. Vincent, K. Wünnemann, Y. Zhang, S.D. Raducan, E. Dotto, N. Chabot, A.F. Cheng, A. Rivkin, O. Barnouin, C. Ernst, A. Stickle, D.C. Richardson, C. Thomas, M. Arakawa, H. Miyamoto, A. Nakamura, S. Sugita, M. Yoshikawa, P. Abell, E. Asphaug, R.-L. Ballouz, W.F. Bottke, D.S. Lauretta, K.J. Walsh, P. Martino, I. Carnelli, The ESA hera mission: Detailed characterization of the DART impact outcome and of the Binary Asteroid (65803) Didymos, Planet. Sci. J. 3 (7) (2022) http://dx.doi.org/10.3847/PSJ/ac6f52, Cited by: 27; All Open Access, Gold Open Access, Green Open Access. URL https://www.scopus.com/inward/record.uri?eid=2-s2.0-85139758968&doi=10.3847%2fPSJ%2fac6f52&partnerID=40&md5=0d2a791a9122b8db1d1f45e63ca2e5df.

[14] W. Wu, C. Wang, Y. Liu, L. Qin, W. Lin, S. Ye, H. Li, F. Shen, Z. Zhang, Frontier scientific questions in deep space exploration, Kexue Tongbao/Chinese Sci. Bull. 68 (6) (2023) 606–627, http://dx.doi.org/10.1360/TB-2022-0667, Cited by: 0. URL https://www.scopus.com/inward/record.uri?eid=2-s2.0-85151051464&doi=10.1360%2fTB-2022-0667&partnerID=40&md5=cce1667a06e143a7dd6d59b5ef816923.

[15] C. Snodgrass, G.H. Jones, The European space Agency's Comet Interceptor lies in wait, Nature Commun. 10 (1) (2019) http://dx.doi.org/10.1038/s41467-019-13470-1, Cited by: 72; All Open Access, Gold Open Access, Green Open Access. URL https://www.scopus.com/inward/record.uri?eid=2-s2.0-85075713434&doi=10.1038%2fs41467-019-13470-1&partnerID=40&md5=13651144c6b5abf64b4f05b51234740d.

[16] D. Moore, J. Leonard, D. Rus, S. Teller, Robust distributed network localization with noisy range measurements, in: SenSys'04 - Proceedings of the Second International Conference on Embedded Networked Sensor Systems, 2004, pp. 50–61, http://dx.doi.org/10.1145/1031495.1031502, Cited by: 784; All Open Access, Green Open Access. URL https://www.scopus.com/inward/record.uri?eid=2-s2.0-27644573932&doi=10.1145%2f1031495.1031502&partnerID=40&md5=7f27dbab21263d69b9052a7537d4f783.

[17] M. André, E. Odelstad, D. Graham, A. Eriksson, T. Karlsson, G. Stenberg Wieser, E. Vigren, C. Norgren, F. Johansson, P. Henri, M. Rubin, I. Richter, Lower hybrid waves at comet 67p/Churyumov-Gerasimenko, Mon. Not. R. Astron. Soc. 469 (2017) S29 – S38, http://dx.doi.org/10.1093/mnras/stx868, Cited by: 22; All Open Access, Bronze Open Access, Green Open Access. URL https://www.scopus.com/inward/record.uri?eid=2-s2.0-85032338055&doi=10.1093%2fmnras%2fstx868&partnerID=40&md5=22bff5298b51d0683929bb14e7739c65.

[18] T. Saiki, Y. Takei, Y. Mimasu, H. Sawada, N. Ogawa, G. Ono, K. Yoshikawa, F. Terui, M. Arakawa, S. Sugita, S.-i. Watanabe, M. Yoshikawa, S. Nakazawa, Y. Tsuda, Hayabusa2's kinetic impact experiment: Operational planning and results, Acta Astronaut. 175 (2020) 362–374, http://dx.doi.org/10.1016/j.actaastro.2020.05.064, Cited by: 14. URL https://www.scopus.com/inward/record.uri?eid=2-s2.0-85086080399&doi=10.1016%2fj.actaastro.2020.05.064&partnerID=40&md5=0954eaa45851a6096fd96e075e378c98.

[19] C.R. Chapman, Space weathering of asteroid surfaces, Annu. Rev. Earth Planet. Sci. 32 (2004) 539–567, http://dx.doi.org/10.1146/annurev.earth.32.101802.120453, Cited by: 200. URL https://www.scopus.com/inward/record.uri?eid=2-s2.0-2342469933&doi=10.1146%2fannurev.earth.32.101802.120453&partnerID=40&md5=d566acb95856b56f38b790efa239b1cf.

[20] D. Lauretta, D. DellaGiustina, C. Bennett, D. Golish, K. Becker, S. Balram-Knutson, O. Barnouin, T. Becker, W. Bottke, W. Boynton, H. Campins, B. Clark, H. Connolly, C. Drouet d'Aubigny, J. Dworkin, J. Emery, H. Enos, V. Hamilton, C. Hergenrother, E. Howell, M. Izawa, H. Kaplan, M. Nolan, B. Rizk, H. Roper, D. Scheeres, P. Smith, K. Walsh, C. Wolner, D. Highsmith, J. Small, D. Vokrouhlický, N. Bowles, E. Brown, K. Donaldson Hanna, T. Warren, C. Brunet, R. Chicoine, S. Desjardins, D. Gaudreau, T. Haltigin, S. Millington-Veloza, A. Rubi, J. Aponte, N. Gorius, A. Lunsford, B. Allen, J. Grindlay, D. Guevel, D. Hoak, J. Hong, D. Schrader, J. Bayron, O. Golubov, P. Sánchez, J. Stromberg, M. Hirabayashi, C. Hartzell, S. Oliver, M. Rascon, A. Harch, J. Joseph, S. Squyres, D. Richardson, L. McGraw, R. Ghent, R. Binzel, M.M.A. Asad, C. Johnson, L. Philpott, H. Susorney, E. Cloutis, R. Hanna, F. Ciceri, A. Hildebrand, E.-M. Ibrahim, L. Breitenfeld, T. Glotch, A. Rogers, S. Ferrone, C. Thomas, Y. Fernandez, W. Chang, A. Cheuvront, D. Trang, S. Tachibana, H. Yurimoto, J. Brucato, G. Poggiali, M. Pajola, E. Dotto, E.M. Epifani, M. Crombie, C. Lantz, J. de Leon, J. Licandro, J.L.R. Garcia, S. Clemett, K. Thomas-Keprta, S. Van wal, M. Yoshikawa, J. Bellerose, S. Bhaskaran, C. Boyles, S. Chesley, C. Elder, D. Farnocchia, A. Harbison, B. Kennedy, A. Knight, N. Martinez-Vlasoff, N. Mastrodemos, T. McElrath, W. Owen, R. Park, B. Rush, L. Swanson, Y. Takahashi, D. Velez, K. Yetter, C. Thayer, C. Adam, P. Antreasian, J. Bauman, C. Bryan, B. Carcich, M. Corvin, J. Geeraert, J. Hoffman, J. Leonard, E. Lessac-Chenen, A. Levine, J. McAdams, L. McCarthy, D. Nelson, B. Page, J. Pelgrift, E. Sahr, K. Stakkestad, D. Stanbridge, D. Wibben, B. Williams, K. Williams, P. Wolff, P. Hayne, D. Kubitschek, M. Barucci, J. Deshapriya, S. Fornasier, M. Fulchignoni, P. Hasselmann, F. Merlin, A. Praet, E. Bierhaus, O. Billett, A. Boggs, B. Buck, S. Carlson-Kelly, J. Cerna, K. Chaffin, E. Church, M. Coltrin, J. Daly, A. Deguzman, R. Dubisher, D. Eckart, D. Ellis, P. Falkenstern, A. Fisher, M. Fisher, P. Fleming, K. Fortney, S. Francis, S. Freund, S. Gonzales, P. Haas, A. Hasten, D. Hauf, A. Hilbert, D. Howell, F. Jaen, N. Jayakody, M. Jenkins, K. Johnson, M. Lefevre, H. Ma, C. Mario, K. Martin, C. May, M. McGee, B. Miller, C. Miller, G. Miller, A. Mirfakhrai, E. Muhle, C. Norman, R. Olds, C. Parish, M. Ryle, M. Schmitzer, P. Sherman, M. Skeen, M. Susak, B. Sutter, Q. Tran, C. Welch, R. Witherspoon, J. Wood, J. Zareski, M. Arvizu-Jakubicki, E. Asphaug, E. Audi, R.-L. Ballouz, R. Bandrowski, S. Bendall, H. Bloomenthal, D. Blum, J. Brodbeck, K. Burke, M. Chojnacki, A. Colpo, J. Contreras, J. Cutts, D. Dean, B. Diallo, D. Drinnon, K. Drozd, R. Enos, C. Fellows, T. Ferro, M. Fisher, G. Fitzgibbon, M. Fitzgibbon, J. Forelli, T. Forrester, I. Galinsky, R. Garcia, A. Gardner, N. Habib, D. Hamara, D. Hammond, K. Hanley, K. Harshman, K. Herzog, D. Hill, C. Hoekenga, S. Hooven, E. Huettner, A. Janakus, J. Jones, T. Kareta, J. Kidd, K. Kingsbury, L. Koelbel, J. Kreiner, D. Lambert, C. Lewin, B. Lovelace, M. Loveridge, M. Lujan, C. Maleszewski, R. Malhotra, K. Marchese, E. McDonough, N. Mogk, V. Morrison, E. Morton, R. Munoz, J. Nelson, J. Padilla, R. Pennington, A. Polit, N. Ramos, V. Reddy, M. Riehl, S. Salazar, S. Schwartz, S. Selznick, N. Shultz, S. Stewart, S. Sutton, T. Swindle, Y. Tang, M. Westermann, D. Worden, T. Zega, Z. Zeszut, A. Bjurstrom, L. Bloomquist, C. Dickinson, E. Keates, J. Liang, V. Nifo, A. Taylor, F. Teti, M. Caplinger, H. Bowles, S. Carter, S. Dickenshied, D. Doerres, T. Fisher, W. Hagee, J. Hill, M. Miner, D. Noss, N. Piacentine, M. Smith, A. Toland, P. Wren, M. Bernacki, D.P. Munoz, S.-I. Watanabe, S. Sandford, A. Aqueche, B. Ashman, M. Barker, A. Bartels, K. Berry, B. Bos, R. Burns, A. Calloway, R. Carpenter, N. Castro, R. Cosentino, J. Donaldson, J.E. Cook, C. Emr, D. Everett, D. Fennell, K. Fleshman, D. Folta, D. Gallagher, J. Garvin, K. Getzandanner, D. Glavin, S. Hull, K. Hyde, H. Ido, A. Ingegneri, N. Jones, P. Kaotira, L. Lim, A. Liounis, C. Lorentson, D. Lorenz, J. Lyzhoft, E. Mazarico, R. Mink, W. Moore, M. Moreau, S. Mullen, J. Nagy, G. Neumann, J. Nuth, D. Poland, D. Reuter, L. Rhoads, S. Rieger, D. Rowlands, D. Sallitt, A. Scroggins, G. Shaw, A. Simon, J. Swenson, P. Vasudeva,

M. Wasser, R. Zellar, J. Grossman, G. Johnston, M. Morris, J. Wendel, A. Burton, L. Keller, L. McNamara, S. Messenger, K. Nakamura-Messenger, A. Nguyen, K. Righter, E. Queen, K. Bellamy, K. Dill, S. Gardner, M. Giuntini, B. Key, J. Kissell, D. Patterson, D. Vaughan, B. Wright, R. Gaskell, L. Le Corre, J.-Y. Li, J. Molaro, E. Palmer, M. Siegler, P. Tricarico, J. Weirich, X.-D. Zou, T. Ireland, K. Tait, P. Bland, S. Anwar, N. Bojorquez-Murphy, P. Christensen, C. Haberle, G. Mehall, K. Rios, I. Franchi, B. Rozitis, C. Beddingfield, J. Marshall, D. Brack, A. French, J. McMahon, E. Jawin, T. McCoy, S. Russell, M. Killgore, J. Bandfield, B. Clark, M. Chodas, M. Lambert, R. Masterson, M. Daly, J. Freemantle, J. Seabrook, K. Craft, R. Daly, C. Ernst, R. Espiritu, M. Holdridge, M. Jones, A. Nair, L. Nguyen, J. Peachey, M. Perry, J. Plescia, J. Roberts, R. Steele, R. Turner, J. Backer, K. Edmundson, J. Mapel, M. Milazzo, S. Sides, C. Manzoni, B. May, M. Delbo', G. Libourel, P. Michel, A. Ryan, F. Thuillet, B. Marty, The unexpected surface of asteroid (101955) Bennu, Nature 568 (7750) (2019) 55–60, http://dx.doi.org/10.1038/s41586-019-1033-6, Cited by: 320; All Open Access, Green Open Access. URL https://www.scopus.com/inward/record.uri?eid=2-s2.0-85063187846&doi=10.1038%2fs41586-019-1033-6&partnerID=40&md5=ac5de35b8a63e958d27a2d879d61476e.

[21] X. Wang, Y. Jiang, S. Gong, Analysis of the potential field and equilibrium points of irregular-shaped minor celestial bodies, Astrophys. Space Sci. 353 (1) (2014) 105–121, http://dx.doi.org/10.1007/s10509-014-2022-8, URL https://www.scopus.com/inward/record.uri?eid=2-s2.0-84905407809&doi=10.1007%2fs10509-014-2022-8&partnerID=40&md5=fe1dba266971dc8e0343f92e788de1be.

[22] J. Melman, E. Mooij, R. Noomen, State propagation in an uncertain asteroid gravity field, Acta Astronaut. 91 (2013) 8–19, http://dx.doi.org/10.1016/j.actaastro.2013.04.027, URL https://www.scopus.com/inward/record.uri?eid=2-s2.0-84878601920&doi=10.1016%2fj.actaastro.2013.04.027&partnerID=40&md5=9a2b090c7891674c8e3459d14796255a.

[23] H. Li, X. Hou, Feasibility analysis of autonomous orbit determination and gravity-field recovery around asteroids using inter-satellite range data, Aerospace 10 (3) (2023) http://dx.doi.org/10.3390/aerospace10030304, URL https://www.scopus.com/inward/record.uri?eid=2-s2.0-85151520248&doi=10.3390%2faerospace10030304&partnerID=40&md5=be54c7592e71c129801e7d358a126ade.

[24] R. Park, R. Werner, S. Bhaskaran, Estimating small-body gravity field from shape model and navigation data, J. Guid. Control Dyn. 33 (1) (2010) 212–221, http://dx.doi.org/10.2514/1.41585, URL https://www.scopus.com/inward/record.uri?eid=2-s2.0-73949095950&doi=10.2514%2f1.41585&partnerID=40&md5=275525e5b1b396484a260f0834cb8ac1.

[25] Q. Chen, Y. Shen, J. Kusche, W. Chen, T. Chen, X. Zhang, High-resolution GRACE monthly spherical harmonic solutions, J. Geophys. Res. Solid Earth 126 (1) (2021) http://dx.doi.org/10.1029/2019JB018892, Cited by: 16; All Open Access, Green Open Access. URL https://www.scopus.com/inward/record.uri?eid=2-s2.0-85099922833&doi=10.1029%2f2019JB018892&partnerID=40&md5=ed8767c502720c5727a22262b11a4ac7.

[26] R.A. Werner, D.J. Scheeres, Exterior gravitation of a polyhedron derived and compared with harmonic and mascon gravitation representations of asteroid 4769 Castalia, Celest. Mech. Dyn. Astron. 65 (3) (1996) 313–344, Cited by: 685. URL https://www.scopus.com/inward/record.uri?eid=2-s2.0-0000684989&partnerID=40&md5=e97f74e1772bc34c2b82da3ce66cca41.

[27] Z. Zhang, H. Cui, P. Cui, M. Yu, Modeling and analysis of gravity field of 433Eros using polyhedron model method, in: 2nd International Conference on Information Engineering and Computer Science - Proceedings, ICIECS 2010, 2010, http://dx.doi.org/10.1109/ICIECS.2010.5677738, URL https://www.scopus.com/inward/record.uri?eid=2-s2.0-79951653457&doi=10.1109%2fICIECS.2010.5677738&partnerID=40&md5=88bd97a85f45354cfebac009bd4bf2bc.

[28] T. Wen, X. Zeng, Equilibrium points of heterogeneous small body in finite element method, Mon. Not. R. Astron. Soc. 519 (4) (2023) 6077–6087, http://dx.doi.org/10.1093/mnras/stad119, Cited by: 2. URL https://www.scopus.com/inward/record.uri?eid=2-s2.0-85159851510&doi=10.1093%2fmnras%2fstad119&partnerID=40&md5=5945e10bf0560d5fd23001133c92e823.

[29] S. Seriani, P. Gallina, A. Wedler, A modular cable robot for inspection and light manipulation on celestial bodies, Acta Astronaut. 123 (2016) 145–153, http://dx.doi.org/10.1016/j.actaastro.2016.03.020, Cited by: 25; All Open Access, Green Open Access. URL https://www.scopus.com/inward/record.uri?eid=2-s2.0-84961905776&doi=10.1016%2fj.actaastro.2016.03.020&partnerID=40&md5=ce74e9a071bf4b3c160de4de304a5344.

[30] L. Nguyen, T. Harman, C. Fairchild, Swarmathon: A swarm robotics experiment for future space exploration, in: 2019 22nd IEEE International Symposium on Measurement and Control in Robotics: Robotics for the Benefit of Humanity, ISMCR 2019, 2019, http://dx.doi.org/10.1109/ISMCR47492.2019.8955661, URL https://www.scopus.com/inward/record.uri?eid=2-s2.0-85078834477&doi=10.1109%2fISMCR47492.2019.8955661&partnerID=40&md5=3014ec8d24d34c5cd33ca5c78b85a7db.

[31] Y. Huang, S. Wu, Z. Mu, X. Long, S. Chu, G. Zhao, A multi-agent reinforcement learning method for swarm robots in space collaborative exploration, in: 2020 6th International Conference on Control, Automation and Robotics, ICCAR 2020, 2020, pp. 139–144, http://dx.doi.org/10.1109/ICCAR49639.2020.9107997, URL https://www.scopus.com/inward/record.uri?eid=2-s2.0-85087082668&doi=10.1109%2fICCAR49639.2020.9107997&partnerID=40&md5=101387f9d82dce6f7be9915b189535c7.

[32] J. Tejeda, The complete set of thermo-mechanical-radiation methods, simulations and results for a swarm of nanorovers deployed on the moon's surface (lunar zebro mission), in: Proceedings of the International Astronautical Congress, Vol. 2020-October, IAC, 2020, URL https://www.scopus.com/inward/record.uri?eid=2-s2.0-85100915232&partnerID=40&md5=c44ee0ad517d3838bc5e60a905b8a4c6.

[33] J. Thangavelautham, Autonomous robot swarms for off-world construction and resource mining, in: AIAA Scitech 2020 Forum, 1 PartF, 2020, http://dx.doi.org/10.2514/6.2020-0795, URL https://www.scopus.com/inward/record.uri?eid=2-s2.0-85091917090&doi=10.2514%2f6.2020-0795&partnerID=40&md5=62b3b227b17dbb1ae9ef8c557030620f.

[34] M. Carpentiero, M. Sabatini, G. Palmerini, Swarm of autonomous rovers for cooperative planetary exploration, in: Proceedings of the International Astronautical Congress, Vol. 14, IAC, 2017, pp. 9437–9442, URL https://www.scopus.com/inward/record.uri?eid=2-s2.0-85051445086&partnerID=40&md5=638c8cc7728b234c0b2944e8b908a70f.

[35] T. Yoshimitsu, T. Kubota, I. Nakatani, T. Adachi, H. Saito, Micro-hopping robot for asteroid exploration, Acta Astronaut. 52 (2–6) (2003) 441–446, http://dx.doi.org/10.1016/S0094-5765(02)00186-8, Cited by: 79. URL https://www.scopus.com/inward/record.uri?eid=2-s2.0-0037240412&doi=10.1016%2fS0094-5765%2802%2900186-8&partnerID=40&md5=07842db69c801af2a96f7c1f0747db1f.

[36] J. Jiang, X. Zeng, D. Guzzetti, Y. You, Path planning for asteroid hopping rovers with pre-trained deep reinforcement learning architectures, Acta Astronaut. 171 (2020) 265–279, http://dx.doi.org/10.1016/j.actaastro.2020.03.007, Cited by: 48. URL https://www.scopus.com/inward/record.uri?eid=2-s2.0-85081893742&doi=10.1016%2fj.actaastro.2020.03.007&partnerID=40&md5=5f0de638cb56dc8d75fe5547c9798bae.

[37] K. Otto, T.-M. Ho, S. Ulamec, J.-P. Bibring, J. Biele, M. Grott, M. Hamm, D. Hercik, R. Jaumann, M. Sato, S.E. Schröder, S. Tanaka, U. Auster, K. Kitazato, J. Knollenberg, A. Moussi, T. Nakamura, T. Okada, C. Pilorget, N. Schmitz, S. Sugita, K. Wada, H. Yabuta, MASCOT's in situ analysis of asteroid Ryugu in the context of regolith samples and remote sensing data returned by Hayabusa2, Earth Planets Space 75 (1) (2023) http://dx.doi.org/10.1186/s40623-023-01805-8, Cited by: 0; All Open Access, Gold Open Access, Green Open Access. URL https://www.scopus.com/inward/record.uri?eid=2-s2.0-85152688158&doi=10.1186%2fs40623-023-01805-8&partnerID=40&md5=a3915488565e8a1173d24e2c13d79768.

[38] H. Kalita, E. Asphaug, S. Schwartz, J. Thangavelautham, Network of nano-landers for in-situ characterization of asteroid impact studies, IAC, in: Proceedings of the International Astronautical Congress, Vol. 16, 2017, pp. 10382–10392, URL https://www.scopus.com/inward/record.uri?eid=2-s2.0-85048853314&partnerID=40&md5=848345ec7b5f8161eba880ef7400af23.

[39] J. Ehrlich, T. Cichan, A. Gebhardt, A. Marcinkowski, J. Fuller, D. Western, Exploring extreme lunar environments through in-flight swarm deployments, in: IEEE Aerospace Conference Proceedings, vol. 2021-March, 2021, http://dx.doi.org/10.1109/AERO50100.2021.9438173, URL https://www.scopus.com/inward/record.uri?eid=2-s2.0-85111388314&doi=10.1109%2fAERO50100.2021.9438173&partnerID=40&md5=2aa252c72a37739f9173b4f71662da43.

[40] W. Ledbetter, R. Sood, J. Stuart, Expected accuracy of density recovery using satellite swarm gravity measurements, 168, 2019, pp. 2163–2178, URL https://www.scopus.com/inward/record.uri?eid=2-s2.0-85072984637&partnerID=40&md5=6ed4ea762d9dc070db8d459ee31eae41.

[41] M. An, Z. Wang, Y. Zhang, Self-organizing control strategy for asteroid intelligent detection swarm based on attraction and repulsion, Acta Astronaut. 130 (2017) 84–96, http://dx.doi.org/10.1016/j.actaastro.2016.10.038, URL https://www.scopus.com/inward/record.uri?eid=2-s2.0-84994910737&doi=10.1016%2fj.actaastro.2016.10.038&partnerID=40&md5=5acff4feadab965df54309a88f5a24e2.

[42] R. Nallapu, J. Thangavelautham, Spacecraft swarm attitude control for small body surface observation, 169, 2019, pp. 1005–1016, URL https://www.scopus.com/inward/record.uri?eid=2-s2.0-85079129954&partnerID=40&md5=1dfb6f43dbffe8f488b0b44cfb7661f7.

[43] R. Gipe, K. Cui, C. Schulz, J. Balderrama, L. West, J. Cochrane, R. Glaze, G. Lund, M. Salamon, T. Disarro, M. Gupta, Reconfigurable CubeSat swarm, in: AIAA Science and Technology Forum and Exposition, AIAA SciTech Forum 2022, 2022, http://dx.doi.org/10.2514/6.2022-0845, URL https://www.scopus.com/inward/record.uri?eid=2-s2.0-85123452754&doi=10.2514%2f6.2022-0845&partnerID=40&md5=1cdeb0c776632f81767a16d770e5fea1.

[44] R. Nallapu, J. Thangavelautham, Design of spacecraft swarm flybys for planetary moon exploration, in: AIAA Scitech 2020 Forum, vol. 1 PartF, 2020, http://dx.doi.org/10.2514/6.2020-0954, URL https://www.scopus.com/inward/record.uri?eid=2-s2.0-85091938162&doi=10.2514%2f6.2020-0954&partnerID=40&md5=a88808f4f0eb3bc13da4bfc1fe3f8cc0.

[45] R. Teja Nallapu, J. Thangavelautham, Towards end-to-end design of spacecraft swarms for small-body reconnaissance, in: Proceedings of the International Astronautical Congress, IAC, vol. 2019-October, 2019, URL https://www.scopus.com/inward/record.uri?eid=2-s2.0-85079127270&partnerID=40&md5=3779cd4cb2c00f633a96ae9c22e80fa4.

[46] D.J. Barnhart, T. Vladimirova, M.N. Sweeting, Very-small-satellite design for distributed space missions, J. Spacecr. Rockets 44 (6) (2007) 1294–1306, http://dx.doi.org/10.2514/1.28678, Cited by: 155; All Open Access, Green Open Access. URL https://www.scopus.com/inward/record.uri?eid=2-s2.0-38349130284&doi=10.2514%2f1.28678&partnerID=40&md5=e56341f86e96d34ce1421c591617da27.

[47] Z.R. Manchester, M.A. Peck, Stochastic space exploration with microscale spacecraft, in: AIAA Guidance, Navigation, and Control Conference 2011, 2011, Cited by: 22. URL https://www.scopus.com/inward/record.uri?eid=2-s2.0-84880597663&partnerID=40&md5=848034dd49c9be3cfbf53809d35cca08.

[48] L. Weis, M. Peck, Dynamics of chip-scale spacecraft swarms near irregular bodies, in: 54th AIAA Aerospace Sciences Meeting, 2016, http://dx.doi.org/10.2514/6.2016-1468, URL https://www.scopus.com/inward/record.uri?eid=2-s2.0-85007579790&doi=10.2514%2f6.2016-1468&partnerID=40&md5=e37b1991159f4e9668d77403ac014d34.

[49] Y. Gupta, Aakash, H. Agrawal, R. Singh, S. Bhansali, S. Agrawal, S. Khandelwal, V. Kanodia, A. Harshana, A. Vira, Lunar exploration through ChipSats, in: Proceedings of the International Astronautical Congress, Vol. 2020-October, IAC, 2020, URL https://www.scopus.com/inward/record.uri?eid=2-s2.0-85100929823&partnerID=40&md5=99e8c54470036c351e4b67481fcc777f.

[50] D. Ivanov, R. Gondar, U. Monakhova, A. Guerman, M. Ovchinnikov, Electromagnetic uncoordinated control of a ChipSats swarm using magnetorquers, Acta Astronaut. 192 (2022) 15–29, http://dx.doi.org/10.1016/j.actaastro.2021.12.014, Cited by: 1. URL https://www.scopus.com/inward/record.uri?eid=2-s2.0-85121223159&doi=10.1016%2fj.actaastro.2021.12.014&partnerID=40&md5=db9d17cc7f021532d77ed0b85dc4eb31.

[51] M. Shalaby, C.C. Cossette, J.R. Forbes, J. Le Ny, Relative position estimation in multi-agent systems using attitude-coupled range measurements, IEEE Robot. Autom. Lett. 6 (3) (2021) 4955–4961, http://dx.doi.org/10.1109/LRA.2021.3067253, Cited by: 22; All Open Access, Green Open Access. URL https://www.scopus.com/inward/record.uri?eid=2-s2.0-85103277403&doi=10.1109%2fLRA.2021.3067253&partnerID=40&md5=4c82c9342ea501ffac9e273defa6f33a.

[52] C. Savarese, J. Rabaey, J. Beutel, Locationing in distributed ad-hoc wireless sensor networks, in: ICASSP, IEEE International Conference on Acoustics, Speech and Signal Processing - Proceedings, vol. 4, 2001, pp. 2037–2040, Cited by: 557. URL https://www.scopus.com/inward/record.uri?eid=2-s2.0-0034854451&partnerID=40&md5=20d91cd0c284664060783974b9277812.

[53] N.B. Priyantha, H. Balakrishnan, E. Demaine, S. Teller, Poster abstract: Anchor-free distributed localization in sensor networks, in: SenSys'03: Proceedings of the First International Conference on Embedded Networked Sensor Systems, 2003, pp. 340–341, Cited by: 165. URL https://www.scopus.com/inward/record.uri?eid=2-s2.0-18844451022&partnerID=40&md5=5bdca0f20a4b1688dd984babdcdc43ee.

[54] B.K.P. Horn, Closed-form solution of absolute orientation using unit quaternions, J. Opt. Soc. Amer. A Optics Image Sci. Vis. 4 (4) (1987) 629–642, http://dx.doi.org/10.1364/JOSAA.4.000629, Cited by: 3397; All Open Access, Green Open Access. URL https://www.scopus.com/inward/record.uri?eid=2-s2.0-84975553202&doi=10.1364%2fJOSAA.4.000629&partnerID=40&md5=847a301c332bfda213030c9e5ac93f8f.

[55] T. Wen, X. Zeng, C. Circi, Y. Gao, Hop reachable domain on irregularly shaped asteroids, J. Guid. Control Dyn. 43 (7) (2020) 1269–1283, http://dx.doi.org/10.2514/1.G004682, Cited by: 89. URL https://www.scopus.com/inward/record.uri?eid=2-s2.0-85087035191&doi=10.2514%2f1.G004682&partnerID=40&md5=bfdb029af36d32623125082b795c71cd.